Materials Today • Volume xxx, Number xx • xxxx 2022

ELSEVIER

RESEARCH: Original Research

High-stability conducting polymer-based conformal electrodes for bio-/iono-electronics

Bowen Yao [1,2], Luize Scalco de Vasconcelos [3], Qingyu Cui [4], Anne Cardenas [2], Yichen Yan [2], Yingjie Du [2], Dong Wu [2], Shuwang Wu [1,2], Tzung K. Hsiai [4,5], Nanshu Lu [3], Xinyuan Zhu [1,*], Ximin He [2,*]

[1] School of Chemistry and Chemical Engineering, Shanghai Jiao Tong University, Shanghai 200240, China
[2] Department of Materials Science and Engineering, University of California, Los Angeles CA 90095, USA
[3] Department of Engineering Mechanics, University of Texas at Austin, Austin, TX 78712, USA
[4] Department of Bioengineering, University of California, Los Angeles CA 90095, USA
[5] Division of Cardiology, Department of Medicine, University of California, Los Angeles CA 90095, USA

Compared to conventional rigid electronics, polymer-based soft electronics conformal to organisms of irregular shapes have emerged as the next-generation devices, especially benefiting long-term bio-interface interactions that avoid mechanical mismatch and consequent adverse immune responses. Highly conductive poly(3,4-ethylenedioxythiophene):poly(styrenesulfonate) (PEDOT:PSS) has become a promising candidate for building soft conductors/electrodes due to its good conductance, tunable mechanical stiffness, good biocompatibility and facile fabrication into various structures. However, their high instability towards alkaline, reductants and applied voltage has not yet been fully addressed, which inevitably leads to deteriorated performance in complex physiological environments or weather conditions (e.g., humidity). Such intolerances are rooted in unstable electronic/molecular structures of PEDOT caused by de-doping. Besides the low electrical stability, PEDOT:PSS films also exhibit an impaired overall conductance due to its phase separation into PSS-rich and PEDOT-rich domains. Herein, a general and effective coating strategy is proposed, based on a mechanism of simultaneous molecular rejection and electron conjugation, to improve the stability and boost the conductance. Specifically, a reduced-graphene-oxide (rGO) thin layer can not only protect PEDOT: PSS from being de-doped by alkali, bio-reductants and applied voltage through molecular rejection, to maintain its conductivity and ensure stable functions, but also further boost the overall conductance through a bridging effect with its large conjugated domain. This strategy is compatible with various material fabrication techniques, including blade-coating, dip-coating and extrusion-based printing techniques, enabling the fabrication of conductors/electrodes with different structures. Finally, the advantages of excellent stability and high conformability of the composite films as soft conductors have been demonstrated through practical applications in tissue stimulation, electrophysiological recording and proprioceptive hydrogel skins, exhibiting great promise in bio/iono-electronics and human–machine interactions.

* Corresponding authors.
E-mail addresses: Zhu, X. (xyzhu@sjtu.edu.cn), He, X. (ximinhe@ucla.edu).

 https://doi.org/10.1016/j.mattod.2021.12.002

Please cite this article in press as: B. Yao et al., Materials Today (2022), https://doi.org/10.1016/j.mattod.2021.12.002

Keywords: Conducting polymer; Graphene; Stability; Conformal bioelectrode; Conductivity

Introduction

Wearable or implantable soft systems have been advancing quickly for medical diagnosis, surgical implementation and human–machine interactions, and attracted broad interest of neuroscience, biomedical and soft electronic communities [1,2]. Compared to conventional rigid metallic materials which tend to induce adverse immune responses at the implantation sites, non-metallic materials, including ionically conductive polymer and electronic conductive carbon materials (*e.g.,* carbon nanotube and graphene), conducting polymers (CPs) (*e.g.,* poly (3,4-ethylenedioxythiophene) polystyrene sulfonate (PEDOT:PSS)), have been widely reported as the soft conductors or electrodes for bio- or iono-electronics, owing to their merits of high flexibility, lightweightness, and tunable electrical properties through molecular design [3–5]. Polymer-based ionic conductors have been prepared based on several strategies including molecular design of the polymer matrix [6,7], the introduction of passive/active ceramics [8,9] and infiltration with a solvent [10]. Though widely explored for the applications of dye-sensitized solar cells [11,12], batteries [13] and electrocatalysis [8], they still suffer from low conductivities (below 1 S cm^{-1}), which makes them unsuitable as electrodes for bio/iono-electronics. Electronic conductive graphene films exhibit high electronic conductivities (*e.g.,* up to 8000 S cm^{-1}) and excellent mechanical strength (*e.g.,* 800 MPa fracture strength), but usually require a harsh post-treatment process and careful optimization of the fabrication procedure for such a high performance. For example, for the preparation of chemically derived graphene with a high conductivity above 1000 S cm^{-1}, thermal annealing (>900 °C) is usually adopted, thus compromising the processability and limiting its applications [14–19].

Compared to carbon materials, PEDOT:PSS and its derivatives possess good water-solubility, facile processability, and tunable mechanical properties, primarily attributed to the unique properties of the PSS chains that act as both dopant and surfactant for PEDOT, and they can be plasticized by additives such as ionic liquids and glycerol [20,21]. Additionally, PEDOT:PSS has relatively high conductivities (200–7000 S cm^{-1}) and higher electrical stability, compared with other CPs such as polyaniline and polypyrrole prepared with solution-derived methods [22–24]. Owing to these merits, PEDOT:PSS has become a promising material for constructing soft bio-electronics and wearable devices [1,25]. Examples include PEDOT-based multi-channel electrodes fabricated through extrusion-based 3D printing or conventional photolithography for neural-signal recording, muscle stimulation and electrophysiological mapping of atrial fibrillation at cellular resolution [26–29] as well as PEDOT:PSS fibers (380 S cm^{-1}, fracture strength: ~400 MPa) fabricated by wet-spinning as conductive sutures for biomedical applications [14].

Despite the great progress of PEDOT:PSS for bio/iono-electronics, its electrical stability is still not satisfactory, seriously limiting its practical applications for long-termed usages. For example, PEDOT:PSS-based neural recording electrodes became gradually more insulating over time after implantation, leading to an increased cut-off frequency, below which biological signals could not be presented authentically [30]. When serving as stimulation electrodes, PEDOT:PSS would experience deteriorated charge injection and delamination from the substrate, due to its degradation and swelling upon repetitive stimulation [31]. Such a high instability is mainly rooted in the changes of electronic and/or molecular structures through the doping/de-doping process of PEDOT:PSS upon exposure to stimuli, such as reductants, pH and even the applied potential when exposed to electrolytes (Fig. 1a) [32–35]. For example, when exposed to organic amines that contain two or more primary or secondary amines groups (*e.g.,* N,N,N′,N′-tetramethyl-1,2-ethanediamine, TeMEDA), PEDOT:PSS would undergo a sequential electron transfer and deprotonation process, thus resulting in a significant increase in electrical resistance of 550% [33]. Upon treatment with an alkaline solution, PEDOT:PSS films displayed a ~50% decrease in the conductivity from 2156 S cm^{-1} to ~1100 S cm^{-1}, due to the localized and fewer charge carrier of the de-doped PEDOT chains in alkaline environments [34]. Moreover, due to the high hygroscopicity of PSS, PEDOT:PSS was even susceptible to water [36]. Such a low tolerance towards chemicals and voltage, and taking into consideration variable weather conditions and the complexity of physiological environments in living organisms, greatly restricts the working conditions and stability of PEDOT:PSS as wearable and implantable conductors. For instance, human colons exhibit a weak alkaline environment (pH 7.9–8.5) [37]; neurons release dopamine as a neurotransmitter to send signals to other neurons [38]; and animal cells utilize glutathione as efficient bio-reductants to deactivate free radicals and reactive oxidants [39]. Additionally, highly conductive PEDOT:PSS films are usually prepared through post-treatment with polar solvents, where the coiled-like PEDOT:PSS seperates into conductive PEDOT-rich domains and PSS-rich domains [40,41]. The insulating PSS-rich domains separate the conductive PEDOT-rich domains, posing an increase in the square resistance of the electrodes which hinders electron transportation. Therefore, stabilizing PEDOT:PSS without sacrificing their conductance at the electrode-tissue interface is a critical prerequisite of its real-life applications as conductors and/or electrodes with high stability in complex physiological environments or in contact with electrolytes in ionoelectronic devices.

Meanwhile, different from the 1D conductive polymer chains, graphene provides a large conjugated plane for electron conductance, which has been reported to improve the conductivity of PEDOT:PSS as flexible electrodes for solar cells, strain sensors, supercapacitors and tissue engineering [23,42–46]. One particular example is that even the semi-conductive graphene oxide (GO) could improve the conductivity of PEDOT:PSS (from 0.049 to 0.4 S cm^{-2}) by altering the PEDOT:PSS chain conformation and morphology [47]. Despite the great progress, the graphene/PEDOT:PSS composites still suffers from the stability issue derived from the de-doping of PEDOT:PSS in complex chemical and electrical environments. Furthermore, high compatibility with various solution-based fabrication techniques is also highly desirable to construct PEDOT:PSS electrodes with

Please cite this article in press as: B. Yao et al., Materials Today (2022), https://doi.org/10.1016/j.mattod.2021.12.002

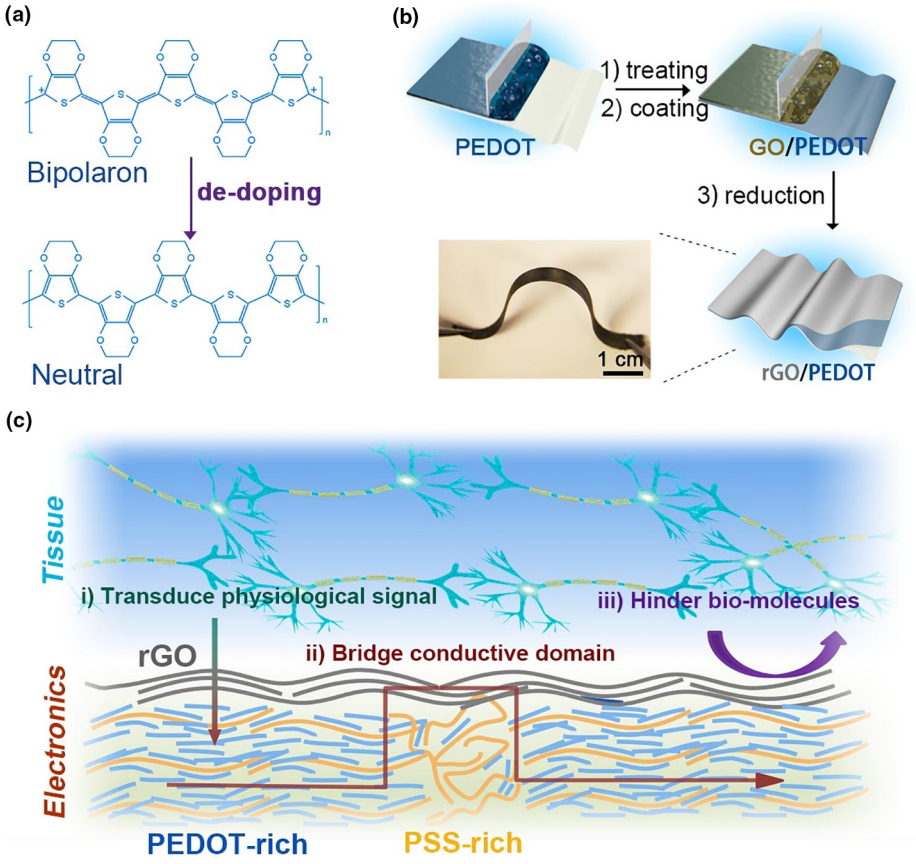

FIG. 1

(a) Molecular structures of PEDOT at the bipolaron and neutral states. (b) Fabrication process and a digital photograph of the rGO/PEDOT:PSS film where PEDOT:PSS was coated onto a polyester substrate and chemically treated to get a highly conductive PEDOT:PSS film. Then, this film was coated with rGO through blade-coating a thin layer of GO followed by chemical reduction. (c) Illustrative schematics of rGO/PEDOT:PSS electrodes at the tissue-electronics interface: the rGO coating could simutaneously transduce electrical signal while rejecting the penetration od bio-molecules through it, in addition to also bridging the highly-conductive PEDOT-rich domains to improve the conductance of PEDOT:PSS electrodes meantime.

arbitrary structures. Herein, a simple strategy was proposed to simultaneously enhance the stability and conductance by taking the PEDOT:PSS films and coating them with a thin layer of reduced graphene oxide (rGO, *e.g.,* 0.5 μm) (Fig. 1b, c). The rGO coating has three functions here: (i) acting as a rejection membrane to protect PEDOT:PSS from being de-doped by alkali or bio-reductants; (ii) providing a large π-conjugated area to bridge the highly conductive PEDOT-rich domains surrounded by lowly conductive PSS-rich domains to boost the conductance of the electrodes; (iii) acting as a stable biological interface to transduce ionic/electronic signals. In detail, graphene has been considered to be the "ultimate reverse osmosis membrane" able to reject most hydrated ions and organic molecules to purify water, because of its two-dimensional (2D) carbon backbone, tunable inter lattice spacing, high mechanical strength and excellent tolerance towards various chemicals [48]. Attributed to the shielding of alkali/bio-molecules by the rGO membrane composed of tightly stacked 2D graphene sheets, the rGO-coated PEDOT:PSS (rGO/CP) films showed highly stable conductances, nearly unaffected by alkali, bio-reductive agents (*e.g.*, glutathione) and water, while all the uncoated PEDOT:PSS electrodes exhibited significant increases in resistances upon exposure to these stimuli (*e.g.,* 30% increment in resistance after immersion in glutathione solution). Meanwhile, different from insulating materials such as polyimide for encapsulation, rGO allowed the ionic/electronic signal transduction at the tissue-electrode interface, which is essential to physiological signal sensing and electrical stimulation for human–machine interactions [49]. The bridging effect of rGO was also confirmed, as revealed by a 10%-25% decrease in the areal resistance compared to the resistance calculated based on a parallel model without the bridging effect, despite the sheet resistances of rGO being ~6 times higher than that of the PEDOT:PSS films. Additionally, the strategy was also compatible with various fabrication techniques, including blade-coating, dip-coating and extrusion-based printing techniques, showing great convenience in the design and construction of conductors or electrodes with high environmental stability and excellent conductance.

Finally, to demonstrate excellent properties, the composite films developed here were successfully employed as soft epidermal electrodes for tissue stimulation (electron-to-ion transduction), including porcine ventricular pacing and Venus flytrap modulating, and for electromyography recording (ion-to-electron transduction) as an excellent soft replacement for rigid

Please cite this article in press as: B. Yao et al., Materials Today (2022), https://doi.org/10.1016/j.mattod.2021.12.002

Ag/AgCl electrodes. Furthermore, to demonstrate good voltage tolerance, the rGO/CP film was also employed as a current collector to successfully deposit an interpenetrating porous graphene network on the film under a negative potential of −1.2 V (*v.s.* saturated calomel electrode (SCE)). This was done in an effort to fabricate low-impedance electrodes with high charge injection capability (CIC) for bioelectronics and hydrogel-based ionic devices. Such an electro-deposition, by contrast, is unachievable on pure PEDOT:PSS electrodes because of the significant decrease in conductivity upon such a negative potential. Using the electrodes with a much lower impedance and good stability, a stretchable surface-capacitive touch panel operatable upon an alternating current (AC) of a wide range of frequencies was fabricated. Compared with resistive strain sensors and triboelectricity-based touching sensors, the capacitive touch panel has a simpler structure requiring fewer electrodes (two or four electrodes for 1D or 2D sensing), promising to be especially useful in multifunctional artificial skins and soft robotics with proprioceptive sensing abilities.

Results and discussion

Preparations and characterizations

To fabricate the CP electrodes, a PEDOT:PSS suspension was first gelated by a 0.06 mol L^{-1} (M) H_2SO_4 solution and blade-casted on to a flexible polyester substrate, followed by a post-treatment and dialysis to remove any excessive additives. Then, the as-prepared PEDOT:PSS films were coated with a thin layer of rGO (0.5 μm in thickness) through blade-casting and chemical reduction (Fig. 1b).

In detail, at first, the addition of 0.06 mol L^{-1} (M) H_2SO_4 could gelate the PEDOT:PSS suspension due to the enhanced interactions among the polymer chains. This led to an increased viscosity with a shear-thinning behavior, beneficial for the fabrication of PEDOT:PSS electrodes with different structures through convenient solution processing methods, such as blade-coating, wet-spinning and 3D printing [14]. Such a gelation process could also be achieved in a relatively less acidic environment by replacing the H_2SO_4 gelator with metal ions, such as Fe^{3+} and Cu^{2+} or ionic liquids, for more convenience based on a similar mechanism [2,50]. Then, the pristine PEDOT:PSS, with a low conductivity (<1 S cm^{-1}), was chemically treated with polar additives H_2SO_4, HI or DMSO (denoted as CP_{SA}, CP_{HI} or CP_D, respectively) to increase its conductivity [40,41,51]. Upon the chemical treatments, all the PEDOT:PSS films underwent molecular configuration changes from a coiled structure to an extended-coiled structure as well as a phase separation between the PSS-rich (light domains) and the PEDOT-rich domains (dark domains) as shown by transmission electron microscopy (TEM) (Fig. 2a and S1) and atomic force microscopy (AFM) (Fig. S2) images, where the dense and highly-conductive PEDOT-rich domains were separated by the less-conductive PSS-rich domains, similar to the phenomenon reported in previous literature [40,41,51]. For comparison, the CP_{HI} showed a more extended structure and a more significant phase separation, while the CP_D showed the least. The CP_{SA} had the highest conductivity of ~1530 S cm^{-1}, while the CP_{HI} and CP_D showed relatively low conductivities of ~630 S cm^{-1} and ~400 S cm^{-1} (Fig. 2b). The high conductivity of the CP_{SA} could be attributed to (i) the high crystallization degree of the PEDOT chains and (ii) the partial removal of PSS chains from the PEDOT:PSS according to Raman spectra (Fig. 2c) [40,52]. First, after the H_2SO_4 treatment, the peak assigned to the $C_\alpha = C_\beta$ stretching vibration of PEDOT chains at 1430 cm^{-1} showed a slightly negative shift to 1425 cm^{-1} with a significant decrease in full width at half maximum (FWHM) from ~ 63.1 to ~ 22.1 cm^{-1}, revealing the expansion of π-conjugated domain and crystallization of PEDOT chains [41].

For comparison, both the peak intensity and FWHM of CP_{HI} and CP_D showed no obvious change. Second, the PSS chains in the CP were partially removed after the H_2SO_4 treatment, as indicated by the obvious decrease of PSS-related peak at 989.6 cm^{-1} for CP_{SA}, while the CP_{HI} and CP_D did not exhibit obvious decrement in the peak intensities. Additionally, the conductivities of CP_{SA}, CP_D and CP_{HI} prepared here were 1–3 times lower than those of semi-transparent CP thin films (*e.g.,* 1233 S cm^{-1} for DMSO-treated counterparts and ~4200 S cm^{-1} for H_2SO_4-treated counterparts with a thickness of <200 nm reported previously) [40,41]. This is potentially a result of insufficient secondary doping of PEDOT:PSS chains, as the films used here were significantly thicker (1–10 μm in thickness), and this could be further improved through future optimization. Finally, the mechanical properties were also studied. The CP films showed Young's moduli of 0.7–1.4 GPa and fracture stress of ~60 MPa (Fig. S3), similar to other semi-crystalline polymers such as Nylon (~0.2–4 GPa) [53] and much lower than those of most metals such as Ag (83 GPa) [54] and Au (76 GPa) [55]. The merits of good softness and high fractural strength were therefore expected to provide the conductor with both conformability and mechanical robustness to cater to bioelectronics and hydrogel-based ionic soft devices [22].

Then, the prepared PEDOT:PSS films were coated with a thin layer of rGO (0.5 μm in thickness), where GO was first coated onto the surface of the CP electrodes via blade-casting, followed by reduction with a 1.5 M HI solution (denoted as rGO/CP_{SA}, rGO/CP_{HI} and rGO/CP_D for the CP_{SA}, CP_{HI} and CP_D counterparts, respectively) [18,56]. The HI treatment could efficiently remove most of the oxygen-containing groups from the GO, as shown by infrared spectra (IR) and X-ray photoelectron spectroscopy (XPS). In IR spectra, the bands associated with the C-O (~1095 cm^{-1}) and C-O-C (1260 cm^{-1}) vibrations significantly decreased after chemical reduction (Fig. S4) [57]. In XPS, the epoxy-, carbonyl-, and carboxyl-related peaks (at 286.6, 287.9 and 289.1 eV, respectively) decreased significantly relative to the peak of the conjugated C–C/C=C bonds (at 284.6 eV), indicating the partial recovery of the graphitic conjugated domain of rGO (Fig. 2d and S4) [56]. This phenomenon was also confirmed by the Raman spectra, as shown by the significant increment of the intensity ratio of D-band (at ~ 1331 cm^{-1}) to G-band (at 1595 cm^{-1}) from ~1.0 to ~2.25 after the reduction (Fig. S4). The micro-morphologies were also studied. All the rGO/CP films showed a uniform coating of rGO layer on to the surface of the CP film, as revealed by the cross-sectional SEM images (Fig. 2e and S4) and spatial distribution of the sulfur elemental (derived from the thiophene unit of the PEDOT chain) in the energy dispersive spectroscopy (EDS) (Fig. 2f and S5), and exhibited similar surface morphologies with wrinkles in the lateral size of

Please cite this article in press as: B. Yao et al., Materials Today (2022), https://doi.org/10.1016/j.mattod.2021.12.002

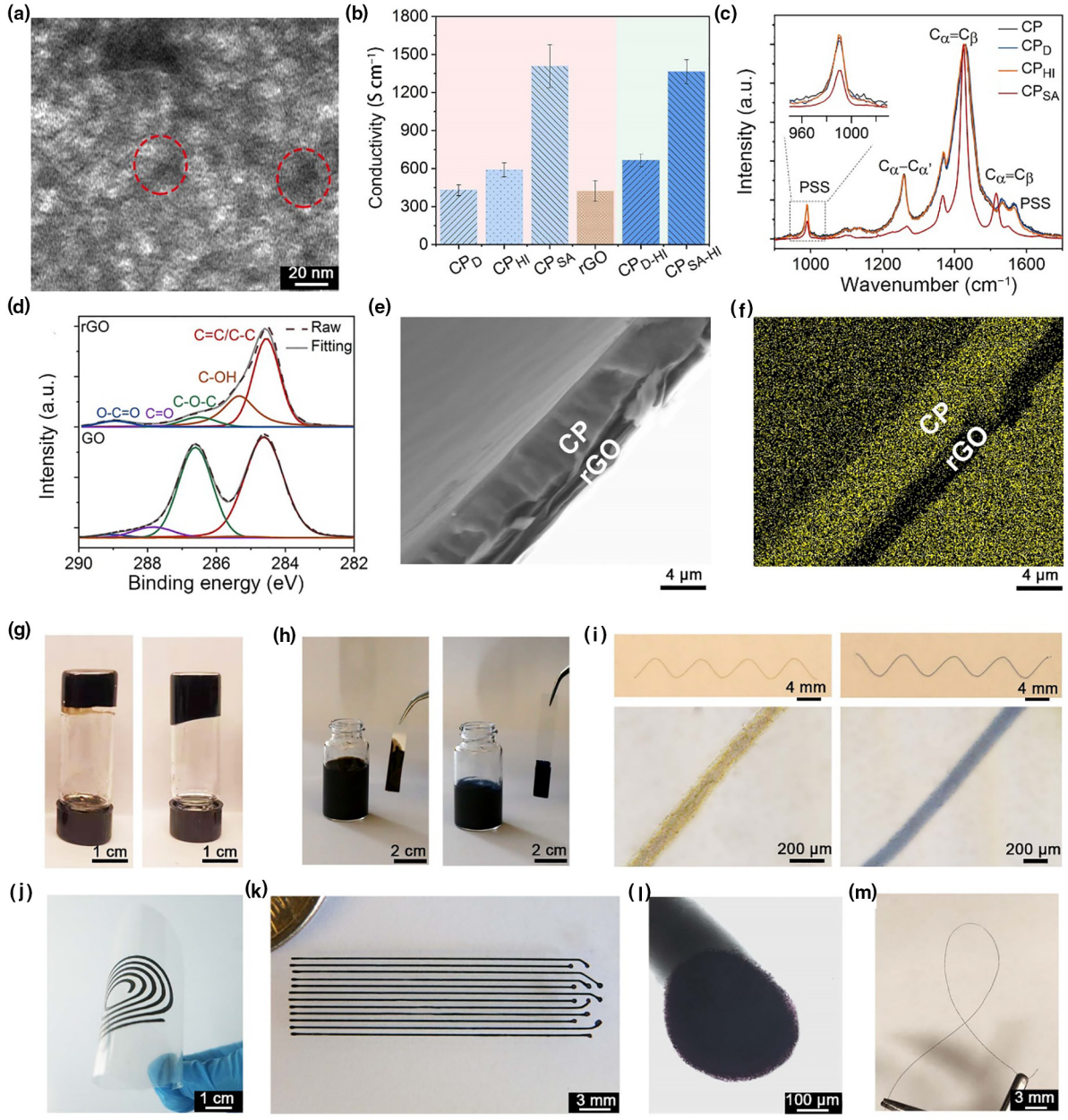

FIG. 2

(a) TEM images of conducting polymer (CP) film prepared by HI treatments, showing the phase separation of PEDOT: PSS. The dark regions marked by the red dashed circles indicate the PEDOT-rich domains. (b) Conductivities of CPand rGO electrodes: CP_D, CP_{HI} and CP_{SA} represent the CP electrodes prepared from chemical treatment with DMSO, HI and H_2SO_4, respectively; $CP_{D\text{-}HI}$ and $CP_{SA\text{-}HI}$ represent the obtained CP_D and CP_{SA} electrodes that were further treated with HI solution. (c) Raman spectra of CP films. (d) C1s X-ray photoelectron spectroscopy of GO and rGO film. (e, f) Cross-sectional SEM images of the rGO/CP_{HI} film (e) and the corresponding elemental sulfur distribution by EDS (f). (g–i) Demonstrations of the good processability of the GO and PEDOT:PSS inks: (g) GO (left) and PEDOT (right) inks in glass bottles placed upside down, indicating their high viscosity; (h) GO (left) and PEDOT:PSS (right) inks dip-coated on polyethylene terephthalate (PET) substrates; (i) dried GO and PEDOT:PSS lines fabricated by the extrusion-printing technique. (j-m) Digital photographs of rGO/CP conductor with different structures: (j) a flexible rGO/CP coil on a PET substrate, prepared by the extrusion-printing technique; (k, l) rGO/CP electrode array with selective patterning prepared by the extrusion-printing techniques on polyester substrate: panel (l) is the microscopic image of the probe head which was covered with a layer of rGO film; (m) rGO/CP fiber prepared by the wet spinning technique.

10–100 μm (Fig. S6), with an average roughness (Ra) of 300–400 nm according to surface profiles (Fig. S6). Furthermore, the interfacial interactions between rGO and CP films were strong enough and could withstand a high shear strength of at least 60 kPa, where no delamination between rGO and PEDOT:PSS occurred before the pure PEDOT:PSS film component fractured upon strain, providing the composite conductor with an excellent mechanical robustness and structural integrality (Fig. S7). Additionally, considering the 1.5 M HI solution was employed here to reduce GO, the effect of HI treatment on the conductivities of the CP_D and CP_{SA} films was also studied. After this extra treatment, an opposite trend was observed (Fig. 2b), where CP_D

Please cite this article in press as: B. Yao et al., Materials Today (2022), https://doi.org/10.1016/j.mattod.2021.12.002

showed an increase of 50% in conductivity (~700 S cm^{-1}), while the CP_{SA} had a slight decrease of ~15% (~1300 S cm^{-1}). This could be explained by the competition between acid-induced phase separation and slight de-doping or secondary doping of PEDOT:PSS in the presence of iodide, where the former usually improves the conductivity while the latter possibly leads to a decrease.

The GO and PEDOT:PSS suspensions had excellent processabilities with both high viscosities and shear-thinning behaviors [1,2,58], thus making them compatible with various materials fabrication methods, including blade-coating, dip-coating and extrusion-based printing techniques (Fig. 2g-i, S8-11 and Video S1). For example, a flexible rGO/CP coil could be prepared by extrusion-printing the PEDOT:PSS and GO successively followed by a HI treatment (Fig. 2j and S9-10). Furthermore, more complex structures, such as the localized encapsulation of PEDOT:PSS electrodes, could also be realized, promising to protect the PEDOT:PSS at the probe head from de-doping without compromising the excellent tunability of the mechanical performance for a seamless interfacial contact with biological tissues of different shapes (Fig. 2k, 2l). Additionally, the conductive, flexible and strong rGO/CP fibers were also obtained by the traditional wet-spinning technique followed by chemical reduction, demonstrating the excellent processabilities of these two inks for the fabrication of knittable conformal conductors (Fig. 2m and S11).

Chemical stabilities, potential tolerances and electrochemical window

To demonstrate the excellent electrical stability of rGO/CP films in reductive, alkaline or moist environments, the electrode resistances were measured before and after treatment with bio-reductants, phosphate buffer solutions (PBS) of different pHs or during direct immersion in water. First, these CP electrodes without rGO coating displayed increased resistances when exposed to respectively three different bio-reductants commonly existing in the biological systems, specifically dopamine, glutathione and sodium ascorbate solutions, where sodium ascorbate induced the largest increase in resistance while dopamine the least (Fig. 3a). For example, the CP_{SA} film had a ~90% and ~40% increment in resistance after the sodium ascorbate and dopamine treatment, respectively. By contrast, all the rGO/CP films (rGO/CP_D, rGO/CP_{HI}, and rGO/CP_{SA}) showed nearly unchanged resistances after the treatment with the same bio-reductant solutions, proving that the rGO films on the surface can efficiently hinder the diffusion of these bio-reductants into the inner PEDOT:PSS films. Second, after being treated with PBS of different pHs (8.0 to 12.0) for 24 h at room temperature, all the pure CP counterparts without rGO protection exhibited a similar trend with resistance increases of ~50% to ~100%, while all the rGO/CP films showed a stable conductance with almost no change, indicating the effective protection of PEDOT and its greatly improved stability in an alkaline environment (Fig. 3b, c). The rGO/CP films also showed excellent long-term stabilities without decreases in conductance after being immersed in a PBS saline (pH = 7.4) for 12 day, while all the pure CP conductors exhibited significant increases of ~100% in resistances (Fig. S14). Third, due to the high hydrophilicity of the PSS chains, the electrical conductances of the CP electrodes were also unstable even when immersed in purified water (Fig. 3d, 3e and S12-13). The resistances of CP electrodes showed an abrupt decrease by 5–10% within the first 2 min, probably caused by the evolved ions via the hydrolysis of PSS chain in the water. With the immersion time prolonged, all the pure CP films exhibited steadily increased resistances. For example, the relative resistance ratio of CP_{SA} immersed in water, relative to the dried CP_{SA}, increased from ~0.85 to ~1.25 when the immersion time increased to 200 min, and the resistance ratio increased from ~0.95 to ~1.0 for CP_{HI} electrodes. By contrast, attributed to the 2D carbon backbone of rGO, the rGO/CP electrodes showed time-independent and nearly constant resistance, revealing the rGO could significantly slow down the diffusion of water, beneficial for improving the stability of PEDOT:PSS electrodes in broad operation conditions.

Then, the effect of rGO thickness on the conductor stability was also studied. All the PEDOT:PSS/rGO films with rGO thicknesses as low as 210 nm showed excellently stable conductance after being immersed in PBS solution of pH = 12 for 24 h. Further decreasing the thickness to ~120 nm resulted in poor tolerance of the rGO/CP conductor towards the alkaline solution as shown by an increase of ~40% in resistance. This is a results of the inhomogeneous coating of rGO on PEDOT:PSS film, limited by the blade coating technique we used here (Fig. S15). Besides the rGO/CP prepared by the blade-coating method, the conductors fabricated through dip-coating, extrusion printing and wet-spinning methods also showed excellent stabilities in conductances after immersion in alkaline or sodium ascorbate solution overnight (Fig. S8 and S11). This showed the outstanding compatibility of the strategy proposed here with different solution-based fabrication methods.

Besides chemical tolerance, the stability of CP and rGO/CP films towards applied potentials were also studied by cy clic voltammogram (CV) and electrochemical impedance spectroscopy (EIS) in a three-electrode system. In the CV curves, a couple of redox peaks corresponding to the de-doping and doping of PEDOT chains evolved at the potential of ~−0.5 V (*vs.* SEC) for the pure CP_D, CP_{HI} and CP_{SA} electrodes, along with significant decreases in current density at potentials below −0.8 V, implying the significant decrease of conductance as the result of the de-doping of PEDOT chains (Fig. 3f and S16). Moreover, according to the EIS, all the pure CP electrodes showed potential-dependent interfacial impedances. Upon a high or mild potential (*e.g.,* 0.8 and 0 V), all the pure CP electrodes showed electrical-double-layer capacitance behaviors (the areal capacitances were estimated to be 25–30 mF cm^{-2}) with low interfacial impedances, and the experimental data could be fitted well with the theoretical model (Fig. 3g, S17 and Table S1). However, upon the application of low potential of −0.8 V, the electrodes exhibited an obvious faradic process (redox reaction) as confirmed by high charge transfer resistances (~300 Ω cm^2), corresponding to the doping/de-doping kinetics (Fig. S17). Furthermore, the experimental data upon −0.8 V, especially in the terms of the real impedance, could not be fitted well with several common equivalent circuits (such as Randle cells with Warburg element) (Fig. S17). The probable reason was the frequency-dependent electronic conductivity of pure PEDOT:PSS film, as the results of two factors: (i) more efficient de-doping of

Please cite this article in press as: B. Yao et al., Materials Today (2022), https://doi.org/10.1016/j.mattod.2021.12.002

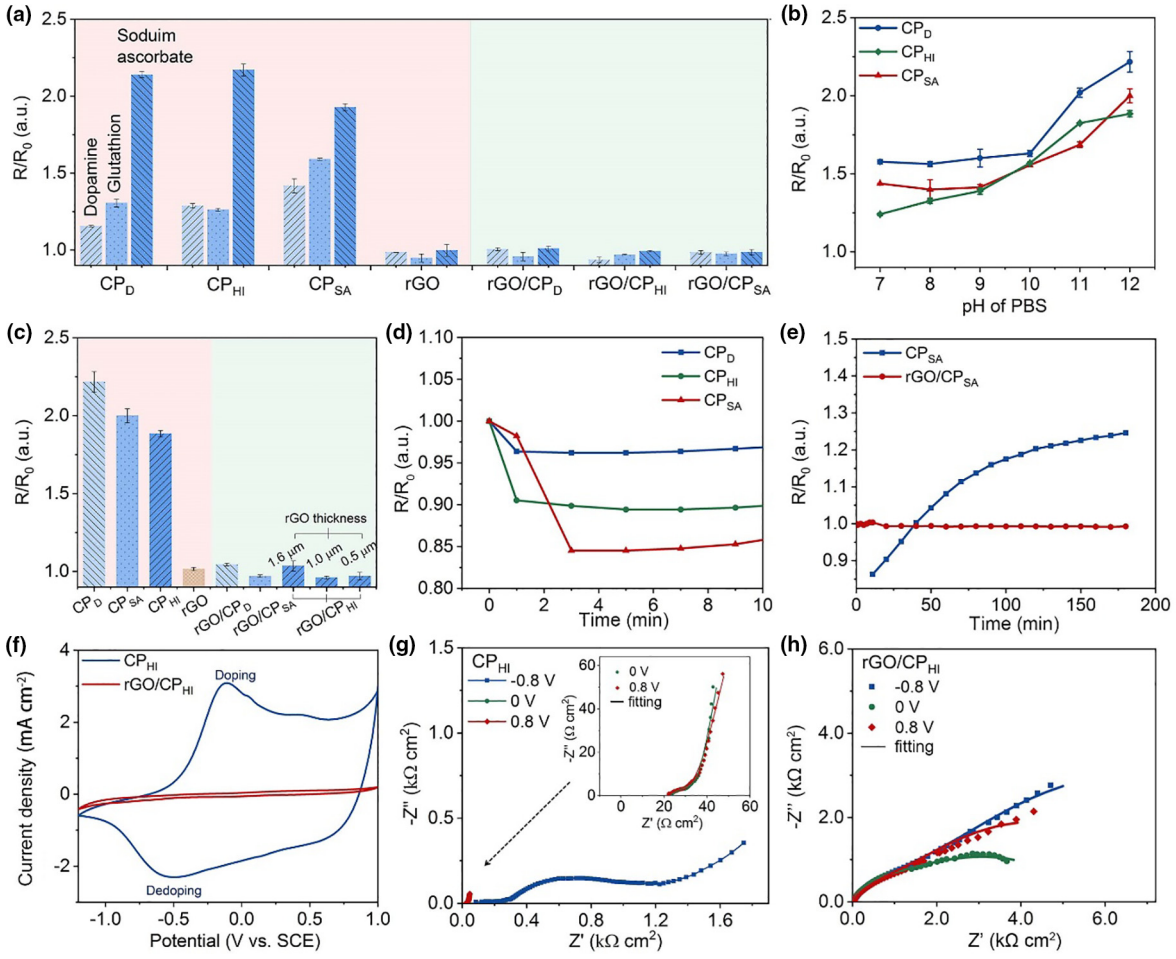

FIG. 3

(a) Resistance changes of the CP, rGO and rGO/CP films after treatment with a 0.1 M dopamine, glutathione or sodium ascorbate solution for 24 h. (b) Resistance changes of the CP films after treated with phosphate buffer solution (PBS) solutions of different pHs for 48 h. (c) Resistance changes of the CP, rGO and rGO/CP electrodes after being treated with a PBS solution of pH = 12 for 48 h. (d, e) Resistance changes in real-time of the CP and rGO/CP films when immersed in a purified water. (f) CVs of CP and rGO/CP_{HI} films as electrodes at a scan rate of 50 mV s^{-1} in a Dulbecco's phosphate buffer saline. (g, h) EIS and corresponding fitting line of the CP_{HI} and rGO/CP_{HI} electrodes at a potential of 0, 0.8 or − 0.8 V (*v.s.* SCE) with an amplitude of 5 mV and a frequency range of 0.1–10^5 Hz in a Dulbecco's phosphate buffer saline.

PEDOT:PSS under low frequency (upon high-frequency, the de-doping was not sufficient as it was limited by ion diffusion); (ii) higher voltage drop across the electrode based on Ohm's law, which led to the further de-doping of the PEDOT:PSS. This assumption could be partially confirmed by the abnormal EIS with the imaginary impedance almost not increasing upon the frequency decreasing from 10^5 to 10^4 Hz (Fig. S17). Though the fitting upon the application of the negative potential was unsatisfactory, the voltage-dependent impedance has already indicated the high dependency of electrochemical reaction and de-doping of the CP electrodes on the applied potential, which is unbeneficial for both the electrical and chemical stability. For comparison, all the rGO/CP electrodes showed stable impedances, almost independent of the applied potential (−0.8 to 0.8 V). Large charge-transfer resistances (200–500 Ω cm^2) and ion diffusion impedances evolved upon low-frequency, as the inevitable but negligible electrochemical side reactions occurred in the Dulbecco's phosphate-buffered saline, corresponding to the low reaction kinetics of minimal redox-active species (Fig. 3h, S17-20 and Table S1).

The high stability of the rGO/CP electrode could be attributed to the excellent ion rejection ability of rGO with a large π-conjugated carbon backbone which significantly hindered the ion diffusion through the coated layer to de-dope the PEDOT:PSS. To prove the excellent ion rejection ability of the rGO, the salt rejection (R_e) ability was measured by permeation tests with a 0.5 M NaCl and purified water as the feed and permeate solutions in an H-type cell (Fig. S21). The feed and permeate solutions showed initial ionic conductivities of 41.8 mS cm^{-1} and 1.48 μS cm^{-1}. When the pure PEDOT:PSS film with a thickness of ~10 μm was used as the separator, the conductivity of the permeate solution increased quickly during the first 1 h and gradually increased to ~20 mS cm^{-1} after 24 h, while that of the feed solution decreased to ~21.9 mS cm^{-1} at the end, corresponding to a NaCl rejection of nearly 0%. For comparison, with the rGO film with a thickness of only ~0.35 μm as the separator, the permeate showed a negligible increase in ionic conductivity after 48 h (2.86 μS cm^{-1}), indicating the excellent rejection ability of rGO towards NaCl (~100%). Therefore, by taking the advantage of closely stacked graphene sheets, the rGO-coating

Please cite this article in press as: B. Yao et al., Materials Today (2022), https://doi.org/10.1016/j.mattod.2021.12.002

strategy could effectively stabilize the PEDOT:PSS electrodes by significantly enhancing its chemical tolerance towards alkaline, bio-reductants and even water, as well as expanding the electrochemical window of the CP conductor in aqueous solutions.

Conductance improvement

Moreover, compared to insulative polymers and inorganic materials (such as parylene, polyimide and SiO_2) as the coating layers, graphene would also provide a large electron-conjugated plane, enabling the electrical connection of the conductive PEDOT-rich domains surrounded by PSS-rich domains for a higher electrical conductance (Fig. 1c and S22). The sheet resistance rather than the conductivity was used to describe the conductance improvement of rGO/CP films to exclude the effect of thickness change considering the relatively lower thickness of the rGO layer (~1.6 μm) compared to the pure CP films (~8.0 μm for CP_D, ~9.0 μm for CP_{HI} and ~4.8 μm for CP_{SA}). In detail, compared to the pure rGO, which has a high sheet resistance of ~12.8 Ω/square, the pure CP films have a relatively low sheet resistance of ~1.9 to ~2.9 Ω/square depending on the chemical treatment methods (Table 1). If no bridging effect would have existed, the sheet resistances of the rGO/CP should be equal to the parallel resistance of its two units, which were calculated to be 2.36, 1.33, and 1.64 Ω/square (Ω/sq^{-1}) for CP_D, CP_{HI}, and CP_{SA}, respectively. Interestingly, the measured sheet resistances of the rGO/CP films were 10–25% lower than the calculated values without the bridging effect. The bridging effect was further confirmed by two phenomena: (i) the CP_{SA} has the lowest thickness among all the three CP electrodes and the rGO/CP_{SA} has the highest improvement ratio; (ii) decreasing the thickness of the rGO layer led to an increase in sheet resistance of pure rGO layer from 12.8 to 105 Ω/square, but the improvement ratio of the overall resistance relative to parallel resistance remained almost unchanged. This could be well explained by the interface effect which gradually dominates with the increase of specific surface as the thickness decreased. Additionally, the higher sheet resistance of rGO compared to those of pure CP also indicated the high electrical conductance is mainly contributed from PEDOT:PSS rather than rGO, and the high stability towards various stimuli as discussed above was indeed derived from the protection of rGO.

Demonstrations of electrical stimulation, bio-sensing, and ionic devices

Attributed to the merits of the rGO/CP films as high-performance bioelectrodes at the tissue-electronics interface, such as the high softness, conformability and expected good bio-compatibility according to previous literature [25,54], several demonstrations have been conducted, including both (1) electric stimulations (electron-to-ion transduction) in heart pacing and plant modulation and (2) electrophysiological sensing on human skin (ion-to-electron transduction). In principle, electric stimulation usually relies on excitable cells such as cardiac muscle cells. In the quiescent state, these cells have a resting electrical gradient across the cell membrane (that is, in a polarized state), which separates the extracellular positive charge and intracellular negative charges. Upon stimulation such as a small current delivered by electrodes through electron-to-ion transduction, the cell membrane will be depolarized and cause the opening of ion channels in the cell membrane, allowing positive ions to flow into the cell. An action potential is therefore produced, which will propagate within the cells and may cause contraction of the cells and tissues. Therefore, electrical stimulation could be used for the therapy of diseases such as muscle spasms, heart failure and neurological dysfunction [59]. The reverse process of electrical stimulation is electrophysiological signal sensing, where the ion flow (in particular, action potential) was measured by electrode through ion-to-electron transductions. One typical example is electroencephalogram recording which provides valuable information for medical diagnosis, health monitoring and human–machine interaction [60].

First, a pair of rGO/CP_{HI} electrodes with an exposed area of ~5 mm^2, coated with a thin layer of ionically-conductive adhesive poly(acrylic acid) hydrogel to facilitate easy and conformal attachment on bio-tissues, were employed for bio-electrical stimulations: in the demonstration of porcine heart pacing, this soft electrode exhibited a pacing voltage threshold of ~3.0 V as the epicardial electrode, comparable with the commonly used rigid gold electrodes (~2.0 V) (Fig. 4a and Video S2). In the demonstration of plant modulation, attributed to its lightweight (only 0.21 mg cm^{-2}), flexibility and conformability, the electrode could be easily attached to the lobes of a Venus flytrap, and thus could promptly switch the Venus flytrap lobes from an open "on" state to a closed "off" state within 2 s upon the application of a threshold voltage of only 1 V (square wave, 2 Hz), lower than that needed by porous Au electrodes (1.5 V) reported in previous literature (Fig. 4b, c and Video S3) [61]. These demonstrations showed the rGO/CP films had the excellent ability to inject electrons into bio-tissues with curved surfaces as well as the advantages of its conformability and softness in avoiding the invasions required by conventional rigid intra- and extracellular methods. Second, the same conformal electrodes with conductive adhesive hydrogels were also attached onto an arm surface and were able to record the electromyography signal with a similar or even higher signal strength than commercial rigid Ag/AgCl electrodes. This showed their potential as an attractive alternative with high performance and desirable conformability,

TABLE 1

Sheet resistances of the rGO, CP and rGO/CP films and the improvement ratios.

Samples	Sheet resistance (Ω sq^{-1})			Improvement ratio (%)	
	rGO	CP	Experimental value	Parallel resistance	
rGO/CP_D	12.9	2.89	1.85	2.36	21.6
rGO/CP_{SA}	12.9	1.48	0.99	1.33	25.5
rGO/CP_{HI}	12.9	1.88	1.32	1.64	19.5
rGO_M/CP_{HI}	33.5	1.88	1.36	1.78	23.6
rGO_T/CP_{HI}	105	1.88	1.41	1.84	23.3

Please cite this article in press as: B. Yao et al., Materials Today (2022), https://doi.org/10.1016/j.mattod.2021.12.002

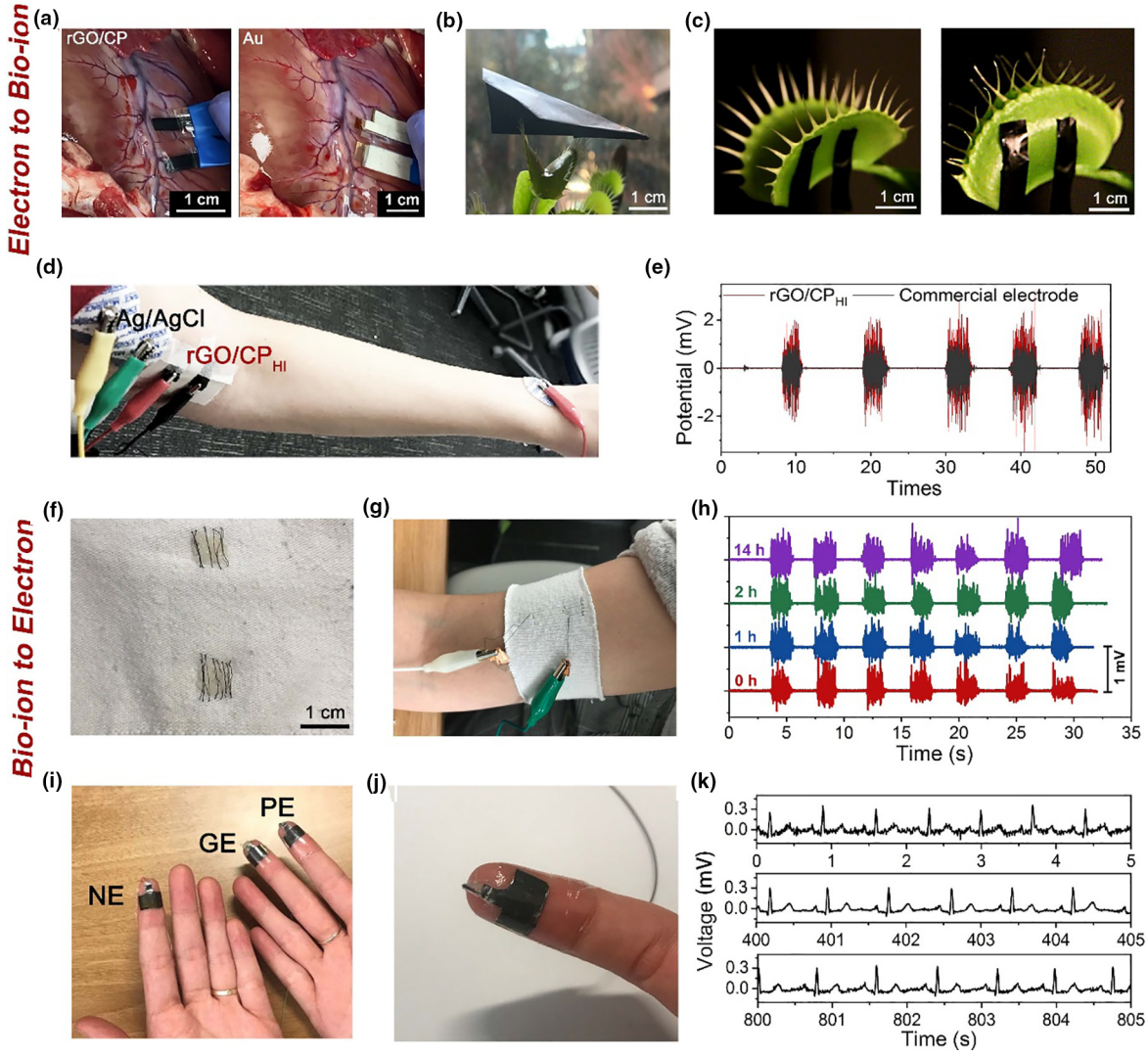

FIG. 4

(a) Electrical stimulation of porcine heart by a pair of adhesive-hydrogel-coated rGO/CP$_{HI}$ (on a polyester substrate) and Au electrodes attached on the epicardium of the right ventricles and epidermis of the lobes. (b) A free-standing rGO/CP/rGO film stand on the cilia of a Venus flytrap, indicating the lightweight of the conductor. (c) Low-voltage modulation of the Venus flytrap from an 'open' to a 'closed' state by a pair of adhesive-hydrogel-coated free-standing rGO/CP$_{HI}$/rGO electrodes attached on the lobes of the Venus flytrap. (d, e) Electromyography recording by a pair of commercially available Ag/AgCl electrodes or rGO/CP$_{HI}$ electrodes (on a polyester substrate) coated with conductive gel attached on the upper arms, with a common ground electrode (Ag/AgCl electrode) on the wrist. (f–h) Demonstration of free-standing rGO/CP fibers for EMG recording: (f, g), digital photograph of rGO/CP fibers, indicating it could be woven into a bandage; (h) the EMG signals recorded at different times. (i–k) Demonstration of rGO/CP$_{HI}$ for ECG recording: (i, j) Digital photographs of rGO/CP$_{HI}$ electrode on fingers, wrapped by a transparent dressing; The electrodes on the index fingers of the left-hand and right-hand as well as middle fingers were negative (NE), positive (PE) and ground electrodes (GE), respectively; (k) Representative ECG signal recorded by the electrodes.

as well as great promise in medical diagnosis and human–machine interaction applications (Fig. 4d, e). Additionally, to demonstrate the benefits of the processibility and structure varieties, flexible rGO/CP fiber electrodes were prepared and were woven into a bandage for an electromyography (EMG) testing with the assistance of a conductive hydrogel paste as an adhesive layer. With a higher wearing comfort compared with rigid Ag/AgCl electrodes, the fiber electrodes could record EMG signals continuously and stably (Fig. 4f-h), uninfluenced by the daily activities including running, cooking, driving and normal rubbing during sleeping, showing great promise in replacing conventional Ag/AgCl electrodes for human–machine-interaction-related applications. Additionally, the rGO/PEDOT:PSS film could also be directly attached to fingers by wrapping them with a transparent dressing for electrocardiogram (ECG) recording. As they exhibited good flexibility and conformability, the dry electrodes could successfully get the ECG signal without the need of either skin pre-treatment (such as mechanical abrasion) or employment of wet conductive hydrogel as an interfacial layer (Fig. 4i–k and S23).

Besides the conformability and softness, the rGO/CP$_{HI}$ electrodes also demonstrated excellent environmental and electrical stability as discussed above. Attributed to the high electrical stability and relatively inert electrocatalytic activities, the electrodes

Please cite this article in press as: B. Yao et al., Materials Today (2022), https://doi.org/10.1016/j.mattod.2021.12.002

were still operable under a higher negative potential (−1.2 V *vs.* SCE) far below that of water electrocatalysis window (around −0.6 to 0.8 V *v.s.* SCE) and were thus successfully employed as current collectors to deposit a porous graphene (PG) matrix from graphene oxide on the rGO surface as revealed by a significant decrease in impedance, as an exemplary demonstration (Fig. 5a–d and S24-25). For comparison, the graphene matrix could not be deposited onto the pure CP_{HI} electrode, probably resulting from the drastic decrease of conductance upon de-doping at the negative potential (Fig. 5d and S25). Charge storage capacity (CSCs) and charge injection capacity (CICs) have been widely employed to evaluate the ion–electron transduction ability of electrodes. Noteworthy, the CSC usually overestimates the performance due to the additional contribution of internal capacitance and pseudocapacitance which are not involved in biological electrical stimulations where a high-frequency alter-

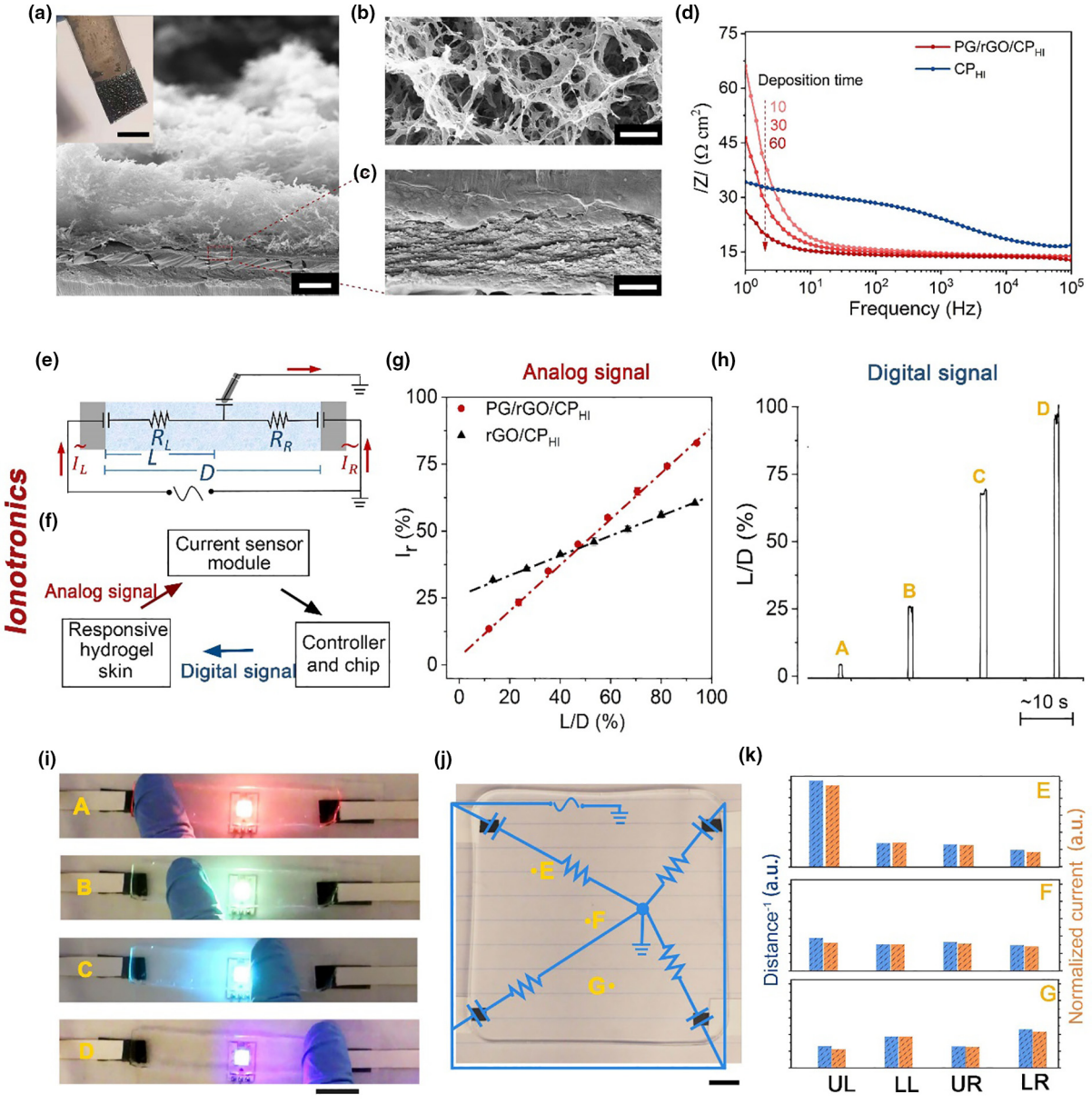

FIG. 5

(a–c) Side-sectional (a, c) and top-sectional (b) SEM images of freeze-dried PG/rGO/CP_{HI} electrode prepared through electrical deposition for 60 s. Scale bar in panels a, b and c are 50, 20 and 2 μm, respectively. The inset in the panel a is the digital photograph of as-prepared PG/rGO/CP_{HI} electrode (scale bar is 1 cm) (d) EIS of freeze-dried PG/rGO/CP_{HI} and CP_{HI} electrodes in Dulbecco's phosphate buffer saline, prepared through electrical deposition of porous graphene on rGO/CP_{HI} or pure CP_{HI} electrodes for different times. (e–i) Demonstration of hydrogel-based 1D touch strip: (e) the equivalent circuit of the 1D touch strip; (f) Data processing and transmittance process of the hydrogel-based touch panel coupled with a digital LED; (g) the plots of current ratio ($I_r = I_R/(I_L + I_R)$) *vs.* the touching location (L/D) by using PR/rGO/CP_{HI} or rGO/CP_{HI} as electrodes; Overall, the currents flowing through the two electrodes were read by current meters (g) and the values were transmitted to a computer and thus the touching state and touching location could be obtained (h) through the analysis of the current values, which were then sent to a microcontroller (Arduino) to control the digital LED depending on the touching state and touching position (i). Scale bar in panel i is 1.5 cm. (j, k) Demonstration of hydrogel-based 2D touch panel: (j) the digital photograph and equivalent circuit of the 2D touch panel made of polyacrylate-based hydrogel and four PG/rGO/CP_{HI} electrodes; (k) Normalized current through the four CP electrodes when the points shown in the panels j were touched by a grounded finger as a conductor. Scale bar in panel j is 1 cm.

Please cite this article in press as: B. Yao et al., Materials Today (2022), https://doi.org/10.1016/j.mattod.2021.12.002

nating current is applied. Interestingly, though with a low CSC (11.6 mC cm^{-2}, only 30% of CP CSC), the resultant PG/rGO/CP electrode showed a much higher CIC of 1.63 mC cm^{-2} than pure CP electrode (1.0 mC cm^{-2}) (Figs. S25 and S26). The high performance could be attributed to the open porous structure of the graphene interpenetrating networks on the surface of the PG/rGO/CP electrode, while the charge injection process was heavily limited by the slow ionic diffusion within the relative dense pure CP electrodes upon high frequency, as confirmed by the more significant CSC deterioration and deviation of CV curve from the rectangular shape for CP electrodes with the increase of scan rate. Therefore, the PG/rGO/CP electrode promise as a stable electrode together with rGO/CP as the conductor for specific neural modulation requiring a much high charge injection.

Additionally, taking the advantage of such PG/rGO/CP_{HI} electrodes, a hydrogel-based touch panel was fabricated. In mechanism, the equivalent circuit of the ionic device is shown in Fig. 5e, where R_L and R_R represent the ionic resistance of the hydrogel, linearly relating with the proximity of the touchpoint to the left and right electrodes (L and R). However, the current ratio ($I_r = I_R/(I_L + I_R)$) was determined not only by the ionic resistance ratio but the interfacial impedance at the hydrogel/electrode interface, thus showing a deviation from the proximity of touchpoint to the two electrodes especially upon low-frequency alternating voltages (<1000 Hz). Compared with rGO/CP_{HI} electrode-based touch panel, the ratios of the currents flowing through the electrodes at the two edges were more consistent with the proximity ratio of the touch-point to the two electrodes for the PG/rGO/CP_{HI} electrode-based touch panel as it exhibits ultralow interfacial impedance within a wide frequency (10–10^5 Hz), thus leading to an improved positioning accuracy (Fig. 5d and g). Then, a proof-of-concept hydrogel skin with touch sensing and displaying ability was demonstrated by integrating the hydrogel panel with a digital LED, where the hydrogel skin could show different colors depending on the touching position through a digital LED, with LabVIEW and Arduino as the controllers (Fig. 5f–I and Video S4). Furthermore, a two-dimensional (2D) touch panel could also be fabricated with four electrodes based on a similar mechanism, which could sense the 2D spatial location of the touchpoint. This shows great promise as smart artificial skins of soft robotics for emerging technologies of 'Internet of Things' and various human–machine interactions.

Conclusion

This work tackled the critical and general instability and conductance issues suffered by CP-based conductors upon exposure to alkali, bio-reductants and applied voltage, which are common physiological environments when in contact with living organisms or with ionic conductors in ionotronic devices, by a general and effective coating strategy. While improving the stability of soft conductors, this strategy can further boost its electrical conductance and maintained its merits of conformality and flexibility which are highly desirable for bio-interfaces. This paradigm has shown great versatility and generalizability in terms of both fabrication and material choices, being compatible with various common electrode fabrication techniques (wet-spinning, extrusion-based printing, *etc.*), while being expected to potentially protect soft conductors/electrodes made of other conducting polymers (polypyrrole, polyaniline, *etc.*) potentially from chemical, electrochemical, and biological stimuli based on a similar mechanism. Fundamentally, this work provides a better understanding of the cause of instability with a clear material degradation mechanism and important insight on the design principle of high-stability soft conductors and electrodes with a wide electrochemical window and long-term functionality especially in water-containing electrolytes, which is a common operational condition for bioelectronics and ionic devices. Practically, beyond the demonstrated high-performance electrical stimulation, electrophysiological signal recording and soft ionic touch panels, this paradigm may be anticipated to advance the emerging technologies of human–machine interactions and 'Internet of Thing' and open up the awaiting market for robotic, surgical and diagnostic implements.

Methods and characterizations

Electrode preparations

Preparation of the CP_{HI} films

PEDOT:PSS suspensions (~13 mg mL^{-1}, Celvios PH1000, Heraeus) were first partially gelated by a 0.06 M H_2SO_4 solution according to previous literature [14], which were then blade-casted onto a flexible polyester substrate (the typical casting thickness is 1.0 mm if not particularly mentioned), and dried at room temperature to get a uniform PEDOT:PSS film. Finally, the resultant films were chemically treated by a HI solution (4.4 M) overnight, dialyzed sufficiently by ethanol to remove the iodine and water sequentially, and then was dried at room temperature to get CP_{HI} films.

Preparation of the CP_{SA} films

Following a similar procedure to that in the preparation of CP_{HI}, uniform PEDOT:PSS films were obtained after blade-casting and drying. Then, they were chemically treated with concentrated H_2SO_4 (18 M) and dialyzed in water, similar to the procedure described in previous literature [41].

Preparation of the CP_D films

Pristine PEDOT:PSS suspensions (~13 mg mL^{-1}) were first treated by DMSO solution by adding 5 wt% DMSO (relative to the mass of suspension) into the suspension, followed by agitation overnight according to previous literature [40]. Then, following a similar procedure to that in the preparation of CP_{HI}, dried PEDOT:PSS films were obtained by blade-casting. Finally, the CP_D films were obtained after dialysis in ethanol to remove the residual DMSO, and thermally annealed at a low temperature of 50 °C for 30 min.

Preparation of the rGO/CP films

The low-defective GO suspension (6 mg mL^{-1}) was prepared by a modified Hummers' method and thermally annealed at 65 °C for 12 h to get a viscous suspension with a shear-thinning behavior [56]. Then, the resultant suspension was blade-coated onto the CP_D, CP_{HI} and CP_{SA} films (typically, the casting thickness is 0.5 mm if not particularly mentioned), dried at room tempera-

Please cite this article in press as: B. Yao et al., Materials Today (2022), https://doi.org/10.1016/j.mattod.2021.12.002

ture, reduced with a 1.5 M HI water solution, dialyzed in ethanol, and finally dried to obtain the corresponding rGO/CP films.

Preparation of the adhesive electrodes

In detail, phosphate-buffered saline (PBS, 1X) solutions containing acrylic acid (10 wt%, relative to solution), N,N′-methylenebis (acrylamide) (Bis) (0.5 wt%, relative to monomer) and 2-hydroxy-2-methylpropiophenone (2.5×10^{-6} wt%, relative to monomer) as photoinitiator were dropped onto the surface of the rGO/CP_{HI} electrodes and gelated under ultraviolet light (Bluewave 200, Dymax) for 30 s.

Preparation of the PG/rGO/CP_{HI} electrodes

rGO/CP_{HI} films with a size of 5 mm × 7 mm were used as current collectors to deposit porous graphene under − 1.2 V (*v.s.* SCE) for 10–60 s in GO suspension (3 mg mL^{-1}) containing 0.1 M $LiClO_4$, followed by electrical reduction at −1.2 V for 600 s in 1 M $LiClO_4$ solution based on the previous literature [62]. For comparison, pure CP_{HI} were also used as current collectors, followed by the same procedure mentioned above.

Preparation of the rGO/CP fibers

CP fibers were prepared by a wet-spinning technique based on the previous literature [63]. In detail, the pristine CP suspensions (~13 mg mL^{-1}) were constantly injected into the coagulation bath (15 M H_2SO_4) at a rate of 0.5 mL min^{-1} from a spinning nozzle with an inner diameter of 0.26 mm (25G). The CP fibers were then transferred into a water bath for dialysis (2 h) and then removed to dry at room temperature GO was then coated onto the CP fibers by drawing the CP fibers through the viscose GO solutions (7 mg mL^{-1}) that were thermally annealed at 65 °C for 12 h beforehand. This process was repeated ten times to a get relative thick coating of GO. Finally, after chemical reduction with a 1.5 M HI water solution, dialysis in ethanol and drying, rGO/CP fibers were obtained.

Extrusion-printing of the rGO/CP electrodes

The rGO/CP micro-electrode was fabricated by an extrusion printer with an extrusion nozzle of 190 μm or 80 μm inner diameter (BIO X™, Cellink). Overall, under the control of g-code command, the PEDOT:PSS was first printed as the first layeron the PET substrate, followed by the printing of GO as the second layer. A high resolution line (*e.g.*, ~150 μm) could be obtained by using an extrusion nozzle with a small inner diameter (80 μm) and optimizing printing speed upon a threshold pressure for continuous extrusion. For PEDOT:PSS, the applied extrusion pressure was 140 kPa, and the printing speed was 10 mm s^{-1}; For GO, the pressure was 35 kPa and the printing speed was 5 mm s^{-1}. Finally, the GO/CP electrodes were treated with a 1.5 M HI solution, followed by dialysis in ethanol and drying at room temperature.

Characterizations of chemical strcutures and micro-morphologies

SEM micrographs were obtained by a field emission scanning electron microscope (Supra 40VP, ZEISS). XPS was tested on a X-ray photoelectron spectrometer (Axis Ultra, Kratos) with an exciting line of Al Kα. Raman spectra were got by a confocal Raman microscope upon a laser of 633 nm (inVia Inspect, Renishaw). The surface roughnesses of different rGO/CP electrodes were measured by a surface profiler (NT9300 Optical Profiler, Bruker) in a vertical-scanning interferometry mode. For AFM characterizations: the thin CP_{SA} and CP_{HI} films were prepared by spin-coating the pristine CP solution on silicon wafers (500 rpm for 60 s), followed by the treatment with a concentrated H_2SO_4 or HI solution (4.4 M) for 20 min and dialysis in ethanol; the thin CP_D film was prepared by spin-coating the pristine CP solution containing 5 wt% DMSO (500 rpm for 60 s), followed by dialysis in ethanol and thermal annealing at 50 °C for 30 min. The AFM images were then taken by atomic force microscope (Dimension FastScan, Bruker) in a tapping mode. For TEM tests: the CP_{SA} and CP_{HI} films were prepared by drop-coating the pristine CP solution on bare Cu grids (2480C, SPI), followed by the treatment with a concentrated H_2SO_4 or HI solution (4.4 M) for 20 min and dialysis in ethanol; the thin CP_D film was prepared by drop-coating the pristine CP solution containing 5 wt% DMSO on a bare Cu grid (2480C, SPI), followed by dialysis in ethanol and thermal annealing at 50 °C for 30 min. The TEM images were then taken by transmission electron microscope (T12 Quick CryoEM, FEI).

Resistance measurements

The resistances of films (width: 0.9 cm, length: 3 cm) were measured by the four-point probe method with a source meter (2450 digital multimeters, Keithley) [64]. Four copper strip electrodes (width, 0.2 cm) as electrodes were attached to the surface of the CP or rGO/CP films for the tests (the spacing of the inner two electrodes was 1.6 cm). The resistances (R), sheet resistances (Rs) and conductivity (σ) were calculated based on eq (1)–(3). For real-time measurements in the water, the four electrodes were replaced by Pt/Au foil electrodes and were encapsulated by transparent tape (Magic tape, 3 M) in avoiding electrochemical side-reactions occurred on the interface of the probes. These electrodes were connected to an electrochemical working station in a four-electrodes mode (CHI660E, CH Instrument). The resistances were obrained by EIS measurment with an initial potential of 0 V (*vs.* SCE) and 5 mV amplitude in the frequency range of 10^5-1 Hz, or in a fixed frequency of 1 Hz for the kinetic tests.

$$R = \frac{V}{I} \tag{1}$$

$$R_s = \frac{V}{I} \times \frac{W}{L} \tag{2}$$

$$\sigma = R_s \times T \tag{3}$$

where I, V, and T are the applied current, the measured voltage, and thickness of the CP films, respectively. W and L are the widths of samples for the test (herein, the width is 0.9 cm) and the spacing of the inner two electrodes (herein, the spacing is 1.6 cm).

Salt rejection of rGO or PEDOT:PSS films

Permeation tests were conducted with a 0.5 M NaCl and purified water as the feed and permeate solution in a H-type cell (Fig. S20), where the ionic conductivities were measured with time. The salt rejections were therefore calculated based on the equation Eq. (4).

Please cite this article in press as: B. Yao et al., Materials Today (2022), https://doi.org/10.1016/j.mattod.2021.12.002

$$R_e = \left(1 - \frac{C_p}{C_F}\right) \times 100\% \approx \left(1 - \frac{S_p}{S_F}\right) \quad (4)$$

Characterization of interfacial interaction

Interfacial interactions between rGO and CP film were characterized by the shear test. In detail, viscous PEDOT:PSS suspensions (~13 mg mL^{-1}, Celvios PH1000, Heraeus) containing 0.06 M H_2SO_4 were blade-casted onto a polyimide substrate (the casting thickness is 1.0 mm, casting area: wide × length = 5 cm × 2.5 cm), and then dried at room temperature. Then, the GO suspension (6 mg mL^{-1}) was also blade-casted onto the polyimide substrate (the overlapping area with CP is 5 cm × 6 mm). The rGO-CP composite film was obtained by treating it with a 1.5 M HI solution followed by dialysis in deionized water. The obtained film was then cut into a strip with a width of 5 mm for the shear test by the dynamic mechanical analyzer (DMA850, TA instrument) at a constant loading rate of 0.5 mm s^{-1} (Fig. S7).

Electrochemical characterizations in a three-electrodes system

A three-electrodes system was employed to study the electrochemical properties of the CP, rGO/CP or PG/GO/CP electrodes through an electrochemical working station (CHI660E, CH Instrument). The CP or rGO/CP electrodes (0.9 × 0.9 cm^2), Pd/Au plate (3 × 1 cm^2) and SCE were employed as working, counter and reference electrodes, respectively. A Dulbecco's phosphate-buffered saline (DPBS) was employed as an electrolyte. CV curves were recorded at a scan rate of 50 mV s^{-1} with an electrochemical window of −1.2–1.0 V (vs. Hg/Hg_2Cl_2). EIS spectra were obtained at an initial potential of 0 V (vs. SCE) with 5 mV amplitude in the frequency range of 10^5-0.1 Hz. Charge injection capacities of different electrodes were measured by the galvanostatic method, where cathodic-lead symmetric square-wave pulses (pulse width: 2 ms) were applied with an interval of 1 ms between cathodic and anodic currents. The cathodic and anodic voltages applied to the electrodes (subtracting the voltage drop across the electrolyte from the total voltage applied) were read at the end of each cathodic and anodic current pulse. The electrochemical window was set to be −0.6–0.8 V (*vs.* SCE) according to previous literature [65,66].

Ex vivo ventricular pacing

rGO/CP_{HI} electrodes (exposed areal of ~5 mm^2) coated with a thin layer of poly(acrylic acid) (PAAc) hydrogel were employed as pacing electrodes. A postmortem study was performed in male Yucatan miniature pigs (S & S Farms, Ranchita, California). All animal studies were approved by the UCLA Office of Animal Research in compliance with the UCLA IACUC protocols. The porcine epicardium was exposed through a thoracotomy, and the epicardium of the right ventricles was attached with rGO/CP_{HI} electrodes. External pacing was conducted after euthanasia, with an amplitude of 2–3 V, a pulse width of 1 ms and a pacing rate of 60 beats per min.

Electrical stimulation of the flytrap

A pair of rGO/CP_{HI} electrodes (exposed areal of ~5 mm^2) coated with a thin layer of PAAc hydrogel was attached to the lower epidermis of the flytrap lobe, which was applied by a square-wave alternating voltage (1.0 V, frequency: 2 Hz) continuously. The reason of choosing alternating voltage is that the voltage threshold for Venus flytrap modulation is lower than that by direct voltage [61].

Electromyograph recording

A pair of commercially available Ag/AgCl electrodes [31] or rGO/CP_{HI} electrodes coated with conductive gel (Abralyt HiCl, Easycap) were employed as recording electrodes attached on the upper arms, with a common ground electrode (Ag/AgCl electrode) on the wrist. The electromyograph signals were recorded by an amplifier (AvatarEEG, Avatar EEG Solutions Inc.) with a 60 Hz notch filter and a 5 Hz high-pass filter.

Electrocardiogram recording

Free-standing rGO/CP_{HI} films were directly attached on the index fingers of the right and left hands and right-hand middle fingers as negative, positive electrodes and ground electrodes, which were then wrapped around with a transparent dressing (Dukal Corp.) for a good electrode/skin contact (impedance ~40 kΩ at 30 Hz)). Neither skin pretreatment nor conductive hydrogel were employed here. The signals were recorded by an amplifier (AvatarEEG, Avatar EEG Solutions Inc.) with a 60 Hz notch filter and a 5 Hz high-pass filter.

Fabrication and testing of touch panel

A strip of PAAc hydrogel containing 1 M NaCl with a size of ~150 mm × 13 mm × 1 mm (length × width × height) was used as the ionic conductor. Either a pair of rGO/CP_{HI} or PG/rGO/CP_{HI} electrodes were attached to the two ends of the hydrogels, and then connected to two current meters (2400 and 2450 digital multimeters, Keithley). The currents flowing through the two electrodes were therefore recorded when a same phase AC voltage (amplitude:1 V) was applied to the two electrodes simultaneously. Meantime, the current values were transmitted to a computer through serial communication and were analyzed by software (LabVIEW) to locate the touching point as represented by a coordinate value (0–100) in real-time. The coordinate values were then sent back and visualized in the term of gradient colors (red to blue, corresponding to the coordinate values of 0–100) by a digital LED (ws2812b) controlled by a microcontroller (Arduino). For 2D touch panel, the fabrication process was similar with that of 1D touch strip, but with a hydrogel with a different size of 9 × 9 cm^2 as ionic conductor and four PG/rGO/CP films as electrodes

CRediT authorship contribution statement

Bowen Yao: Conceptualization, Methodology, Investigation, Visualization, and Writing – original draft. **Luize Scalco de Vasconcelos and Qingyu Cui:** Conceptualization, Methodology, Investigation. **Anne Cardenas:** Writing – review & editing and Funding acquisition. **Yichen Yan and Yingjie Du:** Writing – review & editing. **Dong Wu and Shuwang Wu:** Formal analysis and Investigation. **Tzung K. Hsiai, Nanshu Lu, Xinyuan Zhu:** Funding acquisition, Project administration and Supervision. **Ximin He:** Funding acquisition, Project administration, Supervision and Writing – review & editing.

Please cite this article in press as: B. Yao et al., Materials Today (2022), https://doi.org/10.1016/j.mattod.2021.12.002

Declaration of Competing Interest

The authors declare that they have no known competing financial interests or personal relationships that could have appeared to influence the work reported in this paper.

Acknowledgements

B.Y., Y.Y., Y.D., D.W., S.W., C.A. and X.H. acknowledge the ONR awards N000141712117, N00014-18-1-2314, AFOSR awards FA9550-17-1-0311, FA9550-18-1-0449 and FA9550-20-1-0344, and NSF CAREER award 1724526. C.A. acknowledges the National Science Foundation Graduate Research Fellowship Program under Grant No. DGE-2034835. T. K. H. acknowledges the National Institutes of Health R01HL149808, R01HL159970, and R01HL111437.

Appendix A. Supplementary data

Supplementary data to this article can be found online at https://doi.org/10.1016/j.mattod.2021.12.002.

References

[1] H. Yuk et al., Nat. Commun. 11 (1) (2020) 1604.
[2] V.R. Feig et al., Adv. Mater. 31 (39) (2019) 1902869.
[3] Y. Wang et al., Mater. Today 21 (2) (2018) 186.
[4] K.-Y. Chun et al., Nat. Nanotechnol. 5 (12) (2010) 853.
[5] D. Cai et al., Adv. Mater. 20 (9) (2008) 1706.
[6] P.-H. Wang et al., J. Energy Storage 42 (2021) 103060.
[7] G. Piana et al., Chem. Eng. J. 382 (15) (2020) 122934.
[8] Y.S. Kim, ACS Appl. Polym. Mater. 3 (3) (2021) 1250.
[9] C. Fang, D. Zhang, Chem. Eng. J. 426 (15) (2021) 130793.
[10] J.C. de Haro et al., ACS Sustain. Chem. Eng. 9 (25) (2021) 8550.
[11] S. Galliano et al., Solar RRL 5 (7) (2021) 2000823.
[12] N.A. Rahman et al., Polymer 230 (16) (2021) 124092.
[13] J. Amici et al., Polymers 13 (10) (2021) 1625.
[14] B. Yao et al., Adv. Mater. 29 (28) (2017) 1700974.
[15] G. Xin et al., Science 349 (6252) (2015) 1083.
[16] Z. Xu et al., Adv. Mater. 28 (30) (2016) 6449.
[17] A. Aziz et al., ACS Appl. Nano Mater. 3 (9) (2020) 9385.
[18] Y. Wen et al., Adv. Mater. 29 (41) (2017) 1702831.
[19] K. Pan et al., Nat. Commun. 9 (1) (2018) 5197.
[20] G. Chen et al., Matter 1 (1) (2019) 205.
[21] L. Zhang et al., Nat. Commun. 11 (1) (2020) 4683.
[22] V.R. Feig et al., Nat. Commun. 9 (1) (2018) 2740.
[23] D.L. Gan et al., Adv. Funct. Mater. 30 (5) (2020) 1907678.
[24] M. Berggren, G.G. Malliaras, Science 364 (6437) (2019) 233.
[25] Y. Liu et al., Nat. Biomed. Eng. 3 (1) (2019) 58.
[26] Y. Xiao et al., Sens. Actuators B Chem. 99 (2) (2004) 437.
[27] K.A. Ludwig et al., J. Neural Eng. 8 (1) (2011) 014001.
[28] K.A. Ludwig et al., J. Neural Eng. 3 (1) (2006) 59.
[29] M. Lee et al., Nano Lett. 19 (5) (2019) 2741.
[30] E.M. Thaning et al., J. Biomed. Mater. Res. Part B Appl. Biomater. 93B (2) (2010) 407.
[31] C. Boehler et al., Nat. Protoc. 15 (11) (2020) 3557.
[32] J. Cameron, and Skabara, P. J., Mater. Horiz. 7 (7) (2020) 1759.
[33] T.P.A. van der Pol et al., J. Phys. Chem. C 123 (39) (2019) 24328.
[34] Z. Fan et al., Adv. Energy Mater. 7 (8) (2017) 1602116.
[35] Y. van de Burgt et al., Nat. Mater. 16 (4) (2017) 414.
[36] C. Duc et al., Synth. Met. 238 (2018) 14.
[37] D. Evans et al., Gut 29 (8) (1988) 1035.
[38] S.T. Keene et al., Nat. Mater. 19 (9) (2020) 969.
[39] J. Volk et al., Dent. Mater. 22 (6) (2006) 499.
[40] L.V. Lingstedt et al., Adv. Electron. Mater. 5 (3) (2019) 1800804.
[41] N. Kim et al., Adv. Mater. 26 (14) (2014) 2268.
[42] Y.F. Xu et al., Nano Res. 2 (4) (2009) 343.
[43] H.X. Chang et al., Adv. Funct. Mater. 20 (17) (2010) 2893.
[44] Z.Y. Liu et al., Adv. Mater. 27 (4) (2015) 669.
[45] W.B. Guo et al., ACS Nano 10 (5) (2016) 5086.
[46] G.J. Adekoya et al., Macromol. Mater. Eng. 306 (3) (2021) 2000716.
[47] V.C. Tung et al., J. Am. Chem. Soc. 133 (24) (2011) 9262.
[48] A. Boretti et al., NPJ Clean Water 1 (1) (2018) 5.
[49] E. Song et al., Nat. Mater. 19 (6) (2020) 590.
[50] Y. Wang et al., Sci. Adv. 3 (3) (2017) e1602076.
[51] Y.J. Xia, J.Y. Ouyang, ACS Appl. Mater. Interfaces 2 (2) (2010) 474.
[52] X. Wu et al., Org. Electron. 22 (2015) 160.
[53] E. Zussman, *et al.*, J. Polym. Sci., Part B: Polym. Phys. 44 (10) (2006) 1482.
[54] X.Y. Zhou et al., Phys. Chem. Chem. Phys. 18 (31) (2016) 21508.
[55] S.J. Lee et al., Curr. Appl. Phys. 9 (1) (2009) S75.
[56] M. Zhang et al., Adv. Mater. 27 (42) (2015) 6708.
[57] B.D. Ossonon, D. Bélanger, RSC Adv. 7 (44) (2017) 27224.
[58] R.L. Truby, J.A. Lewis, Nature 540 (7633) (2016) 371.
[59] P.H. Peckham, J.S. Knutson, Annu. Rev. Biomed. Eng. 7 (1) (2005) 327.
[60] A. Zhang, C.M. Lieber, Chem. Rev. 116 (1) (2016) 215.
[61] W.L. Li et al., Nat. Electron. 4 (2) (2021) 134.
[62] K.X. Sheng et al., Sci. Rep. 2 (2012) 247.
[63] J. Zhang et al., J. Mater. Chem. A 7 (11) (2019) 6401.
[64] B. Lu et al., Nat. Commun. 10 (1) (2019) 1043.
[65] S.F. Cogan et al., J. Neural. Eng. 4 (2) (2007) 79.
[66] D.E. Arreaga-Salas et al., ACS Appl. Mater. Interfaces 7 (48) (2015) 26614.

Please cite this article in press as: B. Yao et al., Materials Today (2022), https://doi.org/10.1016/j.mattod.2021.12.002

Supporting information

High-stability conducting polymer-based conformal electrodes for bio-/iono-electronics

Authors: Bowen Yao[1,2], Luize Scalco de Vasconcelos[3], Qingyu, Cui[4], Anne, Cardenas[2], Yichen Yan[2], Yingjie Du[2], Dong Wu[2], Shuwang, Wu[1, 2], Tzung K. Hsiai[4, 5], Nanshu Lu[3], Xinyuan Zhu[1*], Ximin He[2*]

Affiliations:

[1]School of Chemistry and Chemical Engineering, Shanghai Jiao Tong University, Shanghai 200240, China.

[2]Department of Materials Science and Engineering, University of California, Los Angeles CA 90095, USA.

[3]Department of Engineering Mechanics, University of Texas at Austin, Austin, TX 78712, USA

[4]Department of Bioengineering, University of California, Los Angeles CA 90095, USA

[5]Division of Cardiology, Department of Medicine, University of California, Los Angeles CA 90095, USA

[*] E-mail: ximinhe@ucla.edu

xyzhu@sjtu.edu.cn

Supporting Table

Table S1. The fitinng results of electrochemical impedance spectra (EIS) of pure conducting polymer electrodes prepared with HI treatment (CP_{HI}) and reduced-graphene-oxide-coated conduting polymer electrodes (rGO/CP_{HI})

Electrodes	Potentials (V)	R_e (Ω cm^2)	R_{int} (Ω cm^2)	CPE_{int} (T: Ω^{-1} s^P cm^{-2})	CPE_{EDL} (T: Ω^{-1} s^P cm^{-2})	R_{ct} (Ω cm^2)	W_o *or* W_s (R: Ω s^{-P} cm^2)
CP_{HI}	0	22.9	14.5	*T*: 0.0109 *P*: 0.48	*T*: 0.0307 *P*: 0.89	----	----
	0.8	21.8	14.8	*T*: 0.0108 *P*: 0.47	*T*: 0.0268 *P*: 0.85	----	----
	−0.8	275	----	----	*T*: 2.60×10^{-5} *P*: 0.59	317	*R*: 251 *T*: 0.01 *P*: 0.13
rGO/CP_{HI}	0	26.7	----	----	*T*:1.24×10^{-5} *P*:0.81	518	*R*: 1.13×10^{4} *T*: 14.8 *P*: 0.35
	0.8	27.5	----	----	*T*:1.01×10^{-5} *P*:0.83	291	*R*: 5.31×10^{3} *T*: 4.53 *P*: 0.25
	−0.8	27.2	----	----	*T*:1.95×10^{-5} *P*:0.80	320	*R*: 7.33×10^{3} *T*: 8.86 *P*: 0.33

Supporting Figures

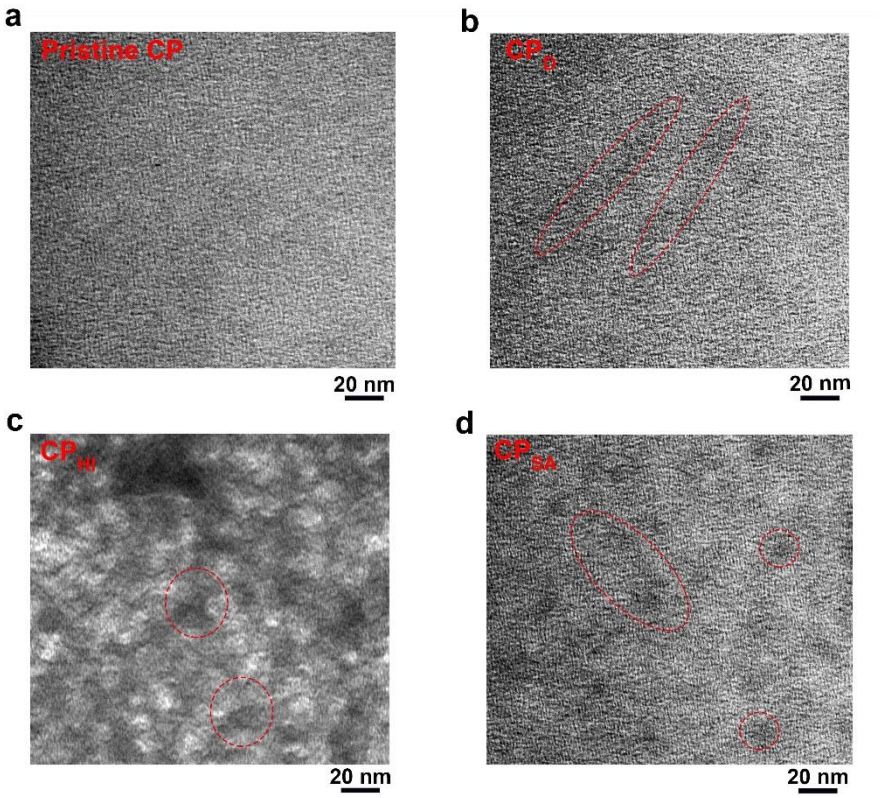

Figure S1. (**a-d**) Transmission electron microscopy (TEM) images of pristine CP film (**a**) and CP film treated by DMSO (**b**), HI (**c**), and H_2SO_4 (**d**). The dark region marked by dashed red circle indicated denser domains than the surrounding, corresponding to the PEDOT-rich domains.

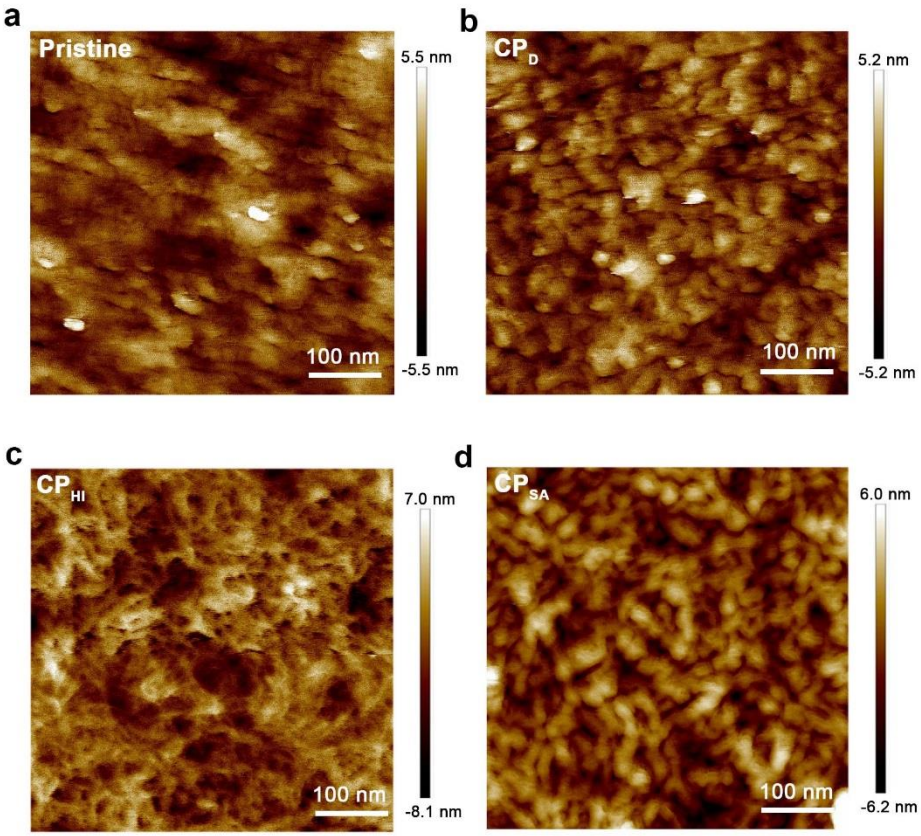

Figure S2. (**a-d**) Atomic force microscopy (AFM) images of pristine CP film (**a**) and CP film treated by DMSO (**b**), HI (**c**), and H_2SO_4 (d). The images were taken in tapping mode.

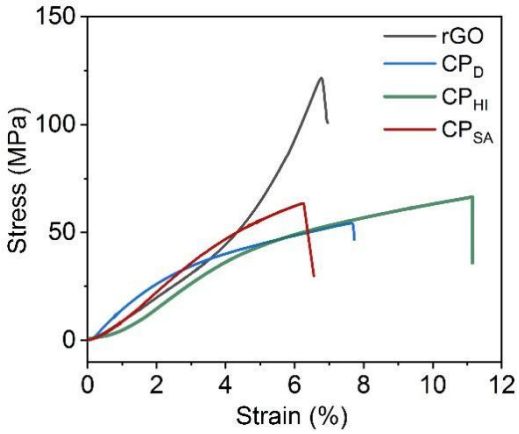

Figure S3. Tensile stress-strain curves of rGO and CP films which were prepared by different chemical treatment methods including DMSO (CP_D), HI (CP_{HI}) and H_2SO_4 (CP_{SA}) treatments.

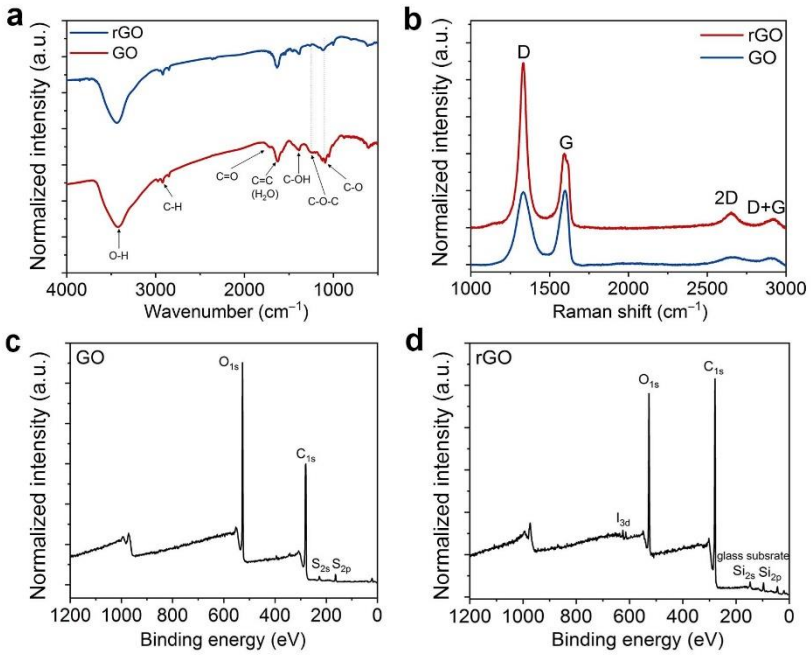

Figure S4. a, Infrared spectra of GO and rGO. The GO and rGO films were grounded and mixed with KBr for the testing. **b,** Raman spectra of GO and rGO films. **c, d,** X-ray photoelectron spectroscopy full survey of GO (**c**) and rGO films (**d**).

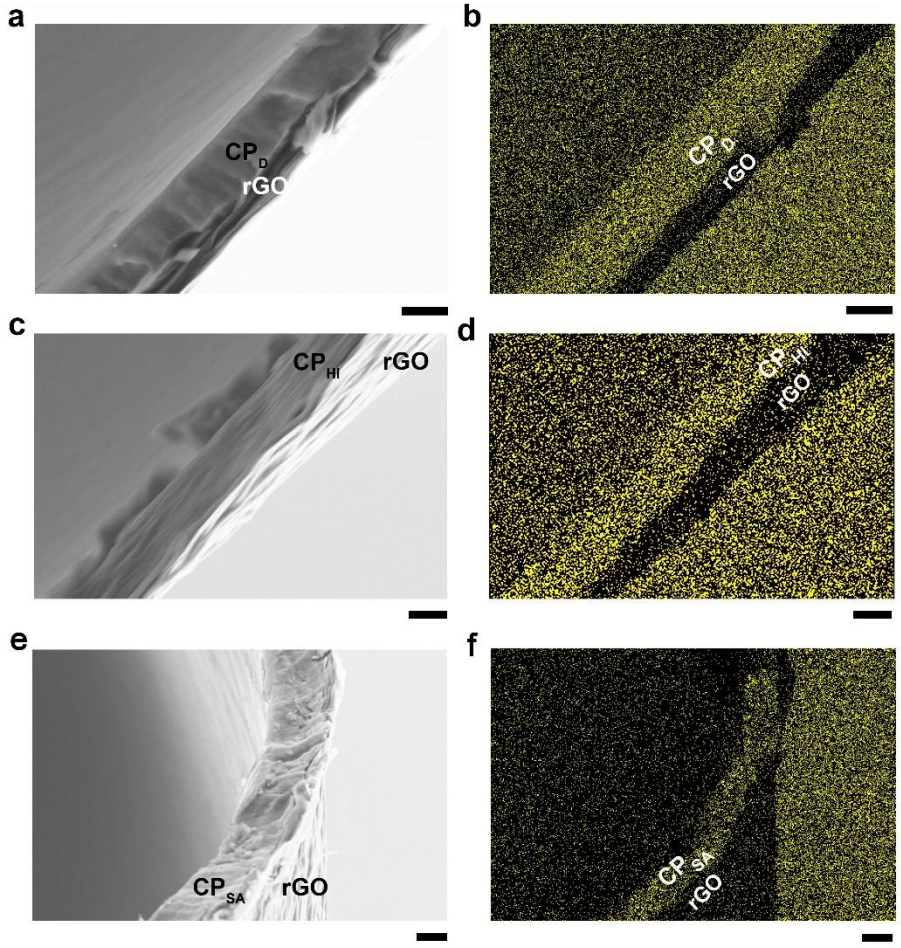

Figure S5. a-f, Cross-sectional SEM images of different rGO/CP films, including rGO/CP_D (**a, b**), rGO/CP_{HI} (**c, d**) and rGO/CP_{SA} (**e, f**). Scale bars in panel a-b, c-d and e-f are 2, 4, and 5 μm, respectively.

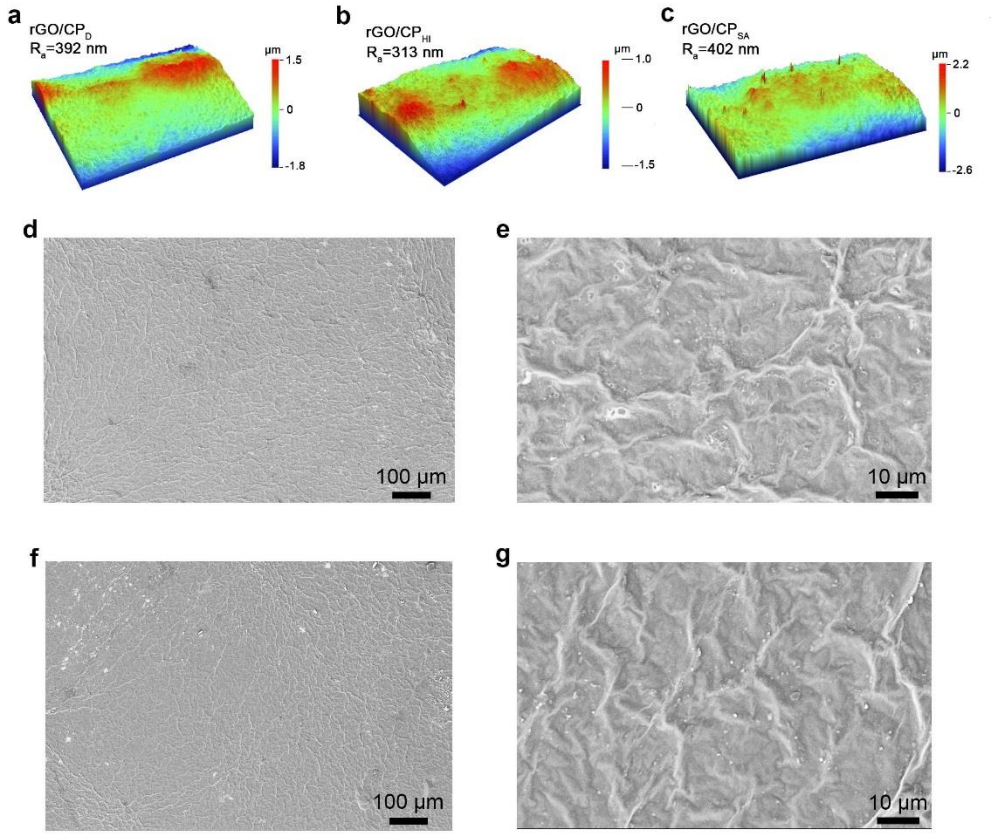

Figure S6. a-c, 3-dimensional height profiles of rGO/CP$_D$ (**a**), rGO/CP$_{HI}$ (**b**) and rGO/CP$_{SA}$ (**c**) films with a sampling area of 1.7 × 2.2 mm^2. **d-g**, SEM images of the rGO/CP$_D$ (**d, e**) and rGO/CP$_{HI}$ (**f, g**) films surface.

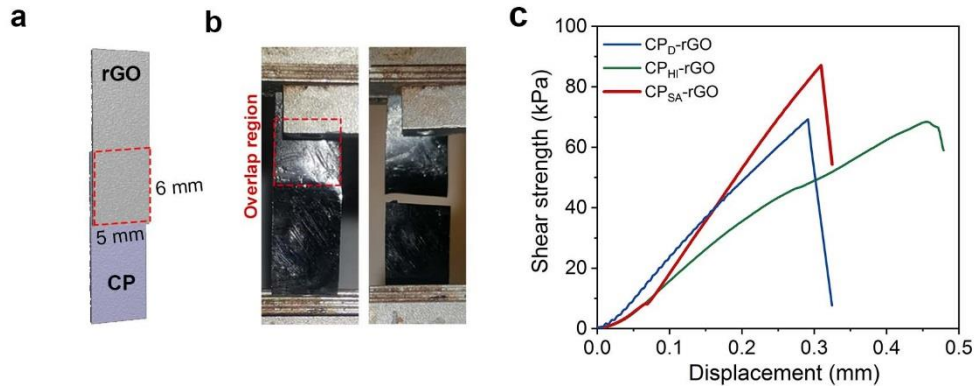

Figure S7. Interfacial interaction between rGO and CP. **a, b**, Illustrative schematics (**a**) and digital photographs (**b**) of the CP-rGO film for the test. **c**, Shear strength-displacement curves of CP-rGO films: CP films were prepared with different chemical treatment methods, including DMSO (CP_D), HI (CP_{HI}) and H_2SO_4 (CP_{SA}) treatments.

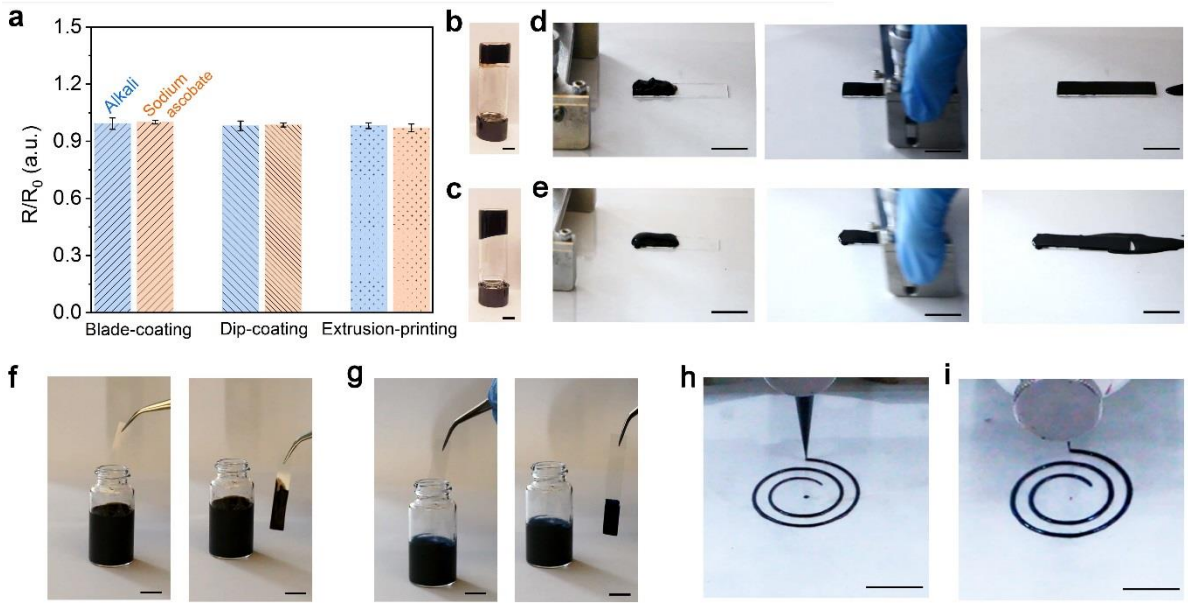

Figure S8. Compatibility of the GO and CP inks with various solution-based fabrication methods. (**a**) Resistance changes of rGO/CP films prepared through blade-coating, dip-coating and extrusion-printing methods. (**b, c**) Digital photographs of GO and CP inks, showing their high viscosities at still. (**d-i**) Digital photographs showing different fabrication procedures of GO (**d, f, h**) and CP (**e, g, i**): blade-coating (**d, e**), dip-coating (**f, g**) and extrusion-printing (**h, i**). Scale bars in b-c, d-e, f-g and h-i are 7 mm, 2.6 cm, 1.4 cm and 2 cm, respectively.

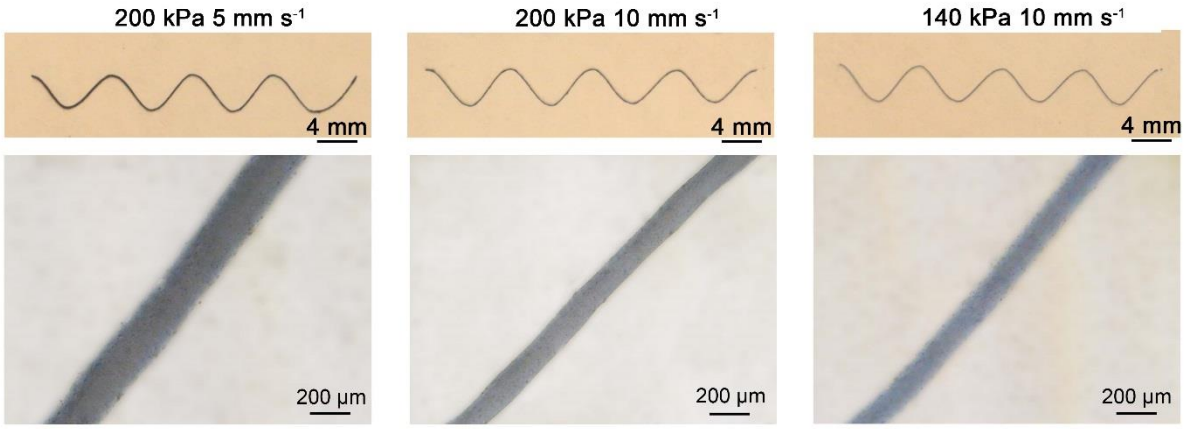

Figure S9. Digital photographs and microscopic images of PEDOT:PSS lines fabricated through the extrusion-printing technique with different extrusion pressure and printing speeds by using an extrusion nozzle of 80 µm in inner diameter.

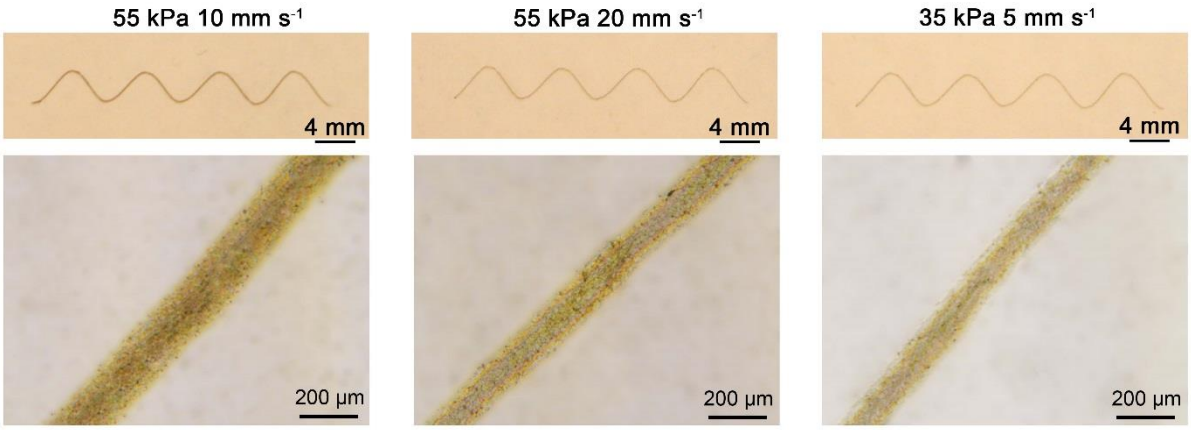

Figure S10. Digital photographs and microscopic images of GO lines fabricated through the extrusion-printing technique with different extrusion pressure and printing speeds by using an extrusion nozzle of 80 μm in inner diameter.

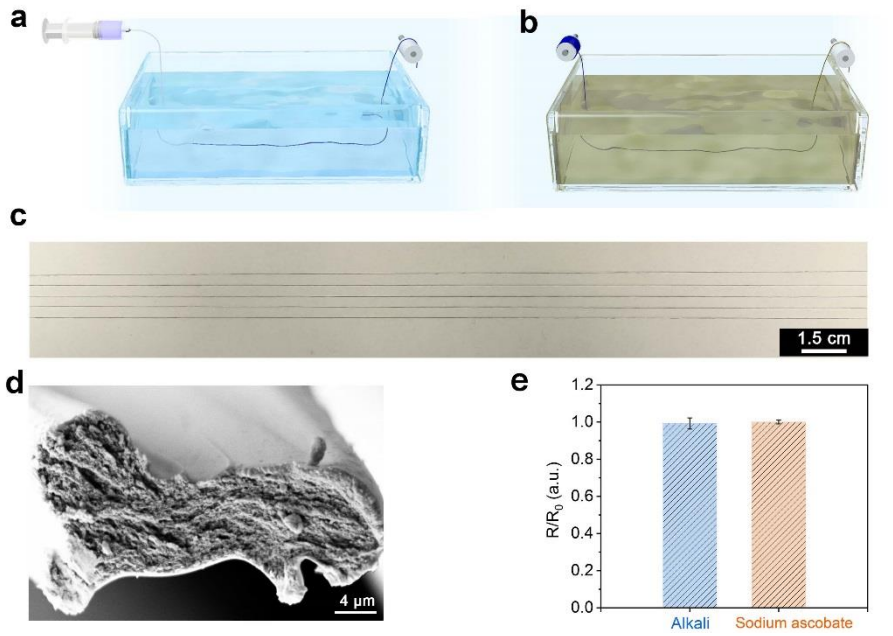

Figure S11. a, Illustrative schematics of preparing CP fibers, where pristine CP suspension was constantly injected into the coagulation bath (15M H_2SO_4) from a spinning nozzle. **b,** Illustrative schematics of preparing GO/CP fibers, where the CP fibers were coated with a layer of GO by repeatedly drawing the CP fibers through viscose GO solution. **c,** Digital photograph of long rGO/CP fibers prepared through the treatment of GO/CP fibers with HI solution, showing the wet-spinning method is suitable for large-scale production. **d,** Cross-sectional images of rGO/CP fiber by scanning electron microscopy. The rGO sheets were uniformly coated on the surface of CP fibers. **e,** Resistance changes of the rGO/CP fibers after being immersed in alkaline (PBS solution, pH =12) or 0.1 M sodium ascorbate solution for 24 hours.

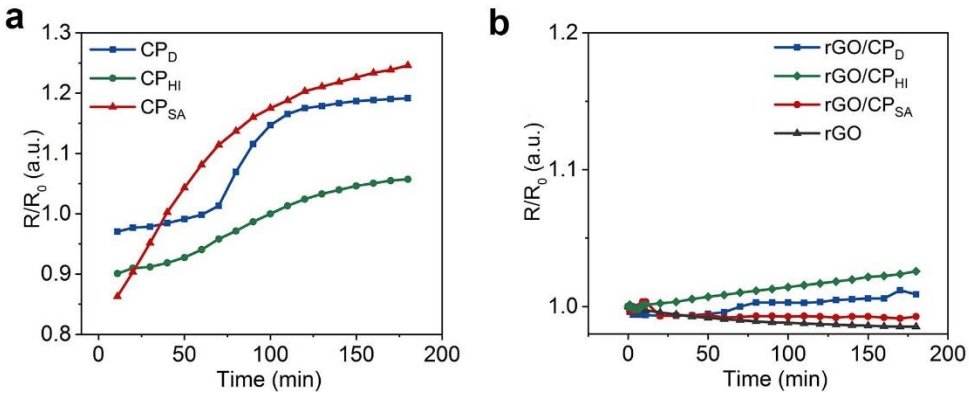

Figure S12. a, b, Resistance changes of pure CP films (**a**) and rGO/CP films (**b**) in real-time when immersed in the purified water. Four-probe measurement was employed to obtain the resistance of the films to eliminate the negative effect of contact resistance between the probe and films.

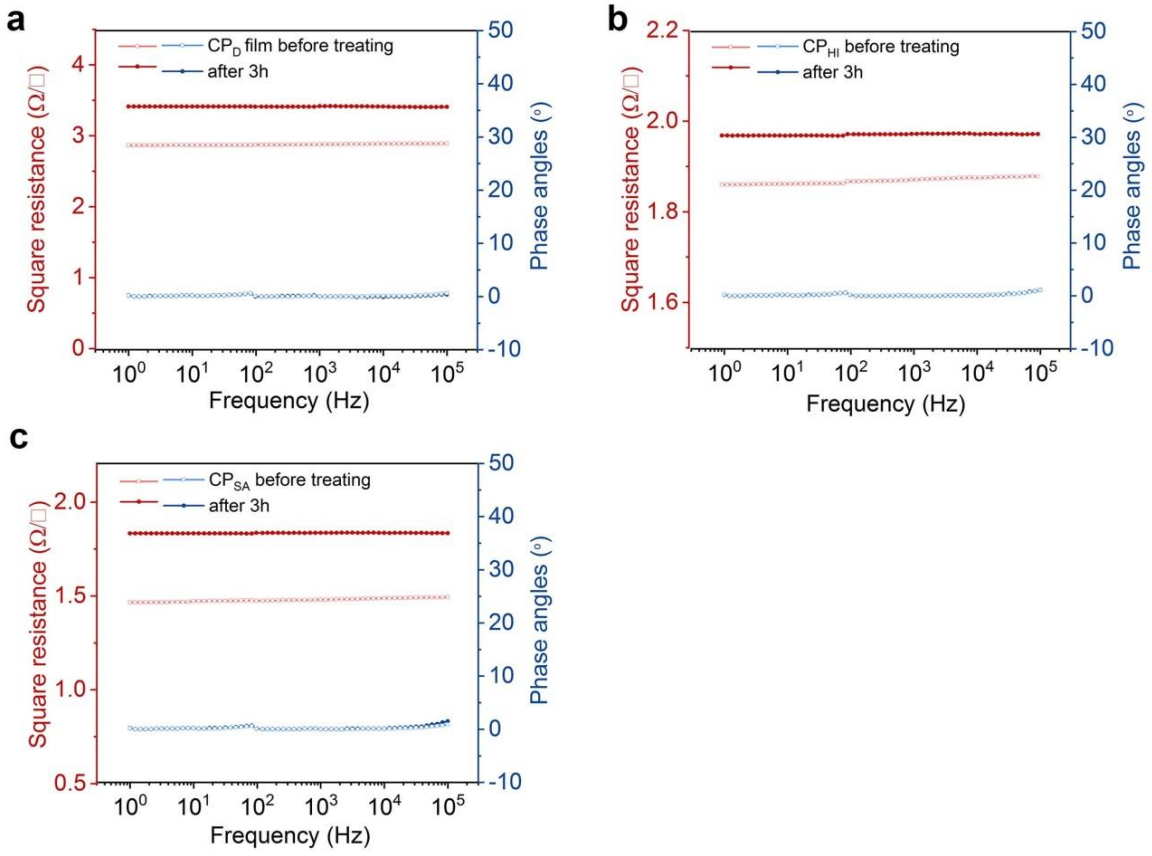

Figure S13. **a-c,** Square resistances and phase angles of the different pure CP films before and after being immersed in the purified water, measured by four-probes impedance method: **a,** CP_D film; **b,** CP_{HI} film; **c,** CP_{SA} film.

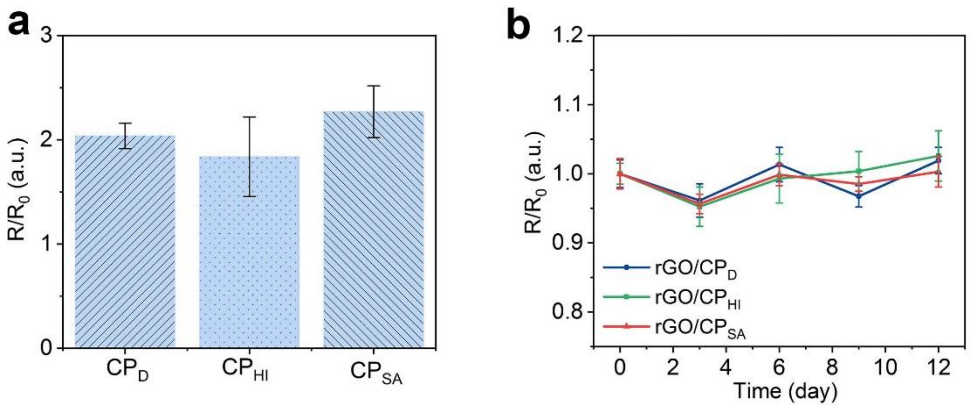

Figure S14. a, b, Resistance changes of CP (**a**) rGO/CP films (**b**) after being soaked in the PBS saline for 12 days

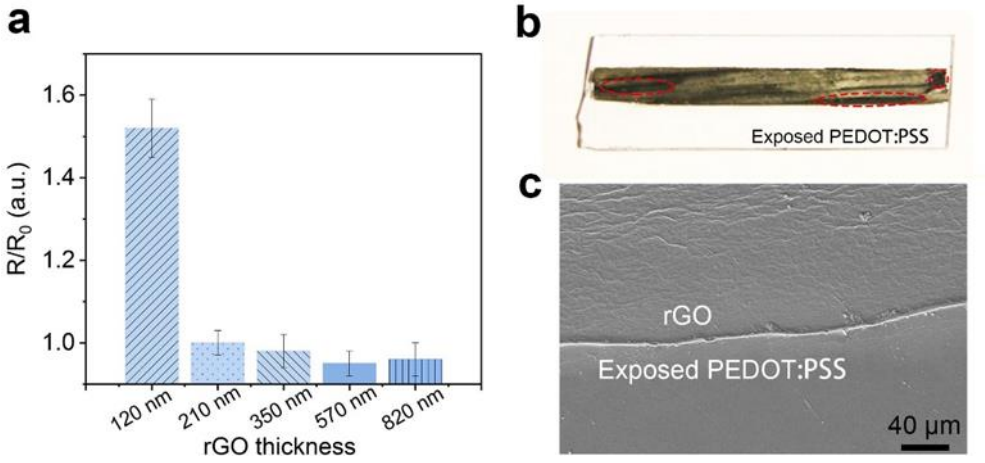

Figure S15. (**a**) The resistance changes of rGO/CP_{HI} films with different rGO thicknesses prepared through blade casting methods by controlling the gap between blade and substrate when coating. (**b**) Digital photograph of rGO/CP_{HI} film with a rGO thickness of ~120 nm. The red dashed circles mark the exposed PEDOT:PSS area, indicating the inhomogeneous coating of rGO. (**c**) SEM images of the boundary region between the unexposed and exposed area of the PEDOT:PSS.

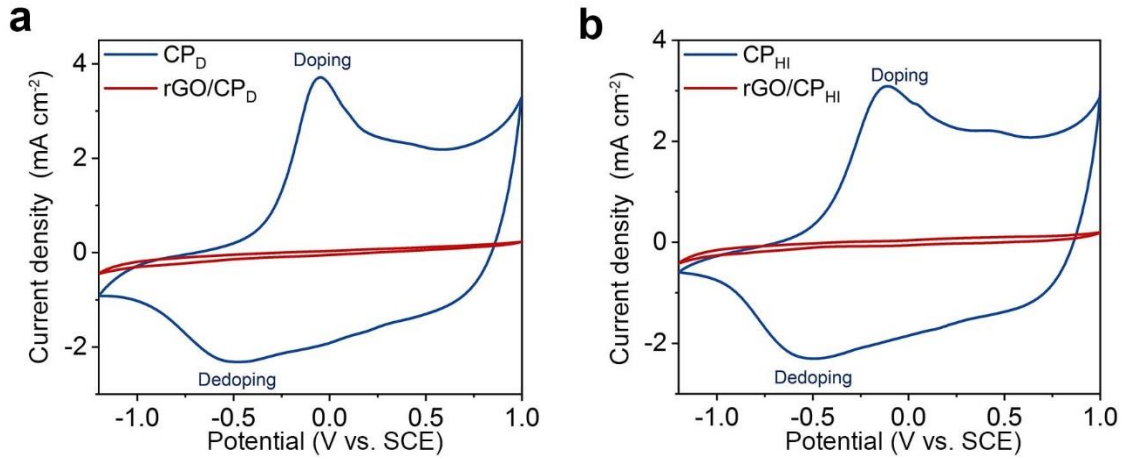

Figure S16. a, b, Cyclic voltammograms of CP_D (**a**) and CP_{HI} (**b**) films as electrodes at a scan rate of 50 mV s^{-1} in a three-electrode configuration with Pt plate as the counter electrode, saturated calomel electrode as the reference electrode, and Dulbecco's phosphate buffer saline as the electrolyte.

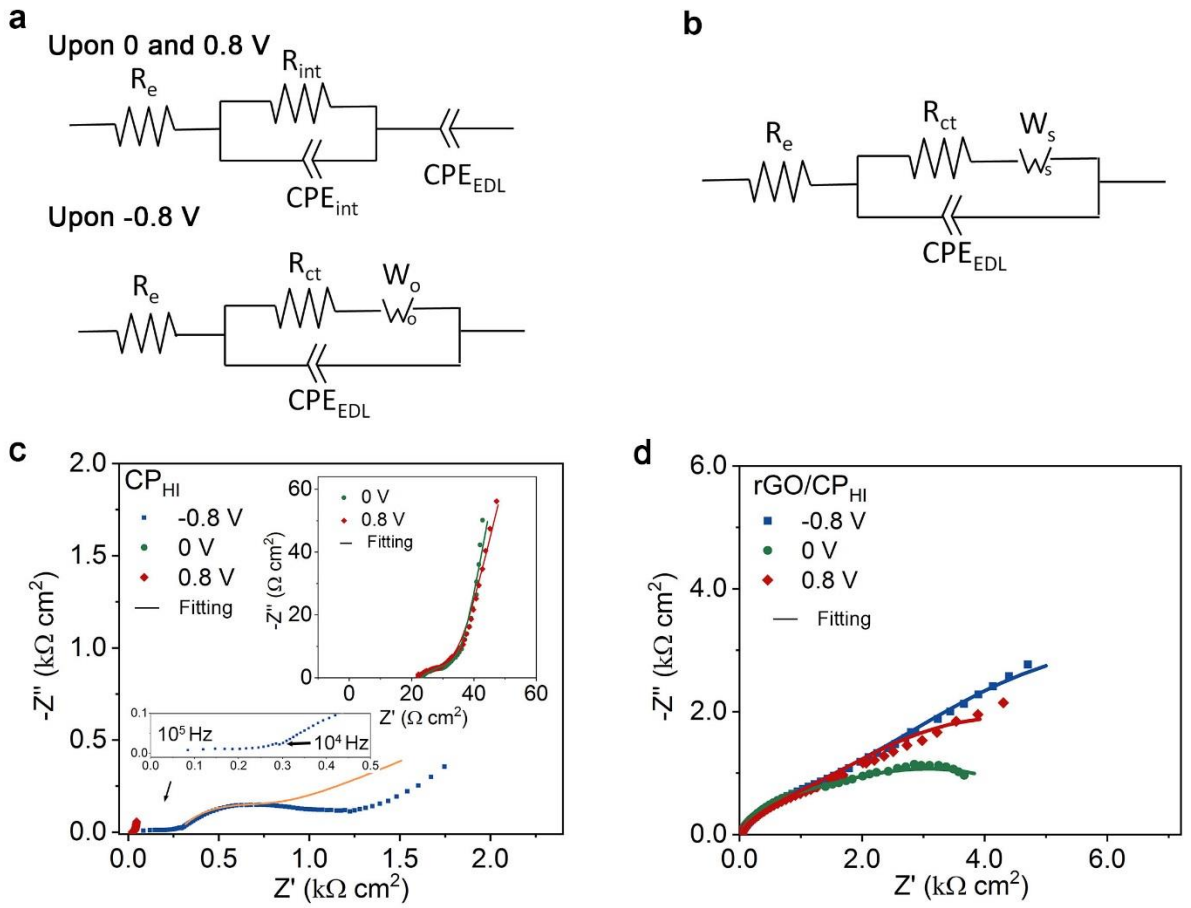

Figure R17. **a, b,** The 'equivalent' circuits of PEDOT:PSS electrodes (**a**) and rGO/CP electrodes (**b**), where R_e represent the overall serial resistance of electrolyte and electrode; is of electrodes; R_{int} and CPE_{int} represent the interfacial resistance and capacitance; R_{ct} and CPE_{EDL} represent charge transfer resistance and double-electric layered capacitance of electrodes; W_s and W_o represent the ionic diffusion impedance with transmissive (Warburg short impedance) and reflective boundaries (Warburg open impedance). The impedances of CPE, W_s and W_o are described by the eq. R1-3, respectively. **c, d,** Electrochemical impedance spectra (EIS) and fitting line of CP_{HI} and rGO/CP_{HI} under different potentials (*vs.* SCE) with 5 mV amplitudes and frequencies of 10^5-0.1 Hz: CP_{HI} (**c**); rGO/CP_{HI} (**d**). The EIS of CP_{HI} at the high-frequency region (10^5-10^4 Hz) upon −0.8 V and the full EIS of CP_{HI} electrode upon 0 and 0.8 V were enlarged in the insets of panel c for clarity. The fitting results are listed in Table R1.

$$Z_{CPE} = \frac{1}{(jT\omega)^p} \qquad (eq.S1)$$

$$Z_{W_s} = \frac{R}{(jT\omega)^p}\tanh([jT\omega]^p) \qquad (eq.S2)$$

$$Z_{W_o} = \frac{R}{(jT\omega)^p}\coth([jT\omega]^p) \qquad (eq.S3)$$

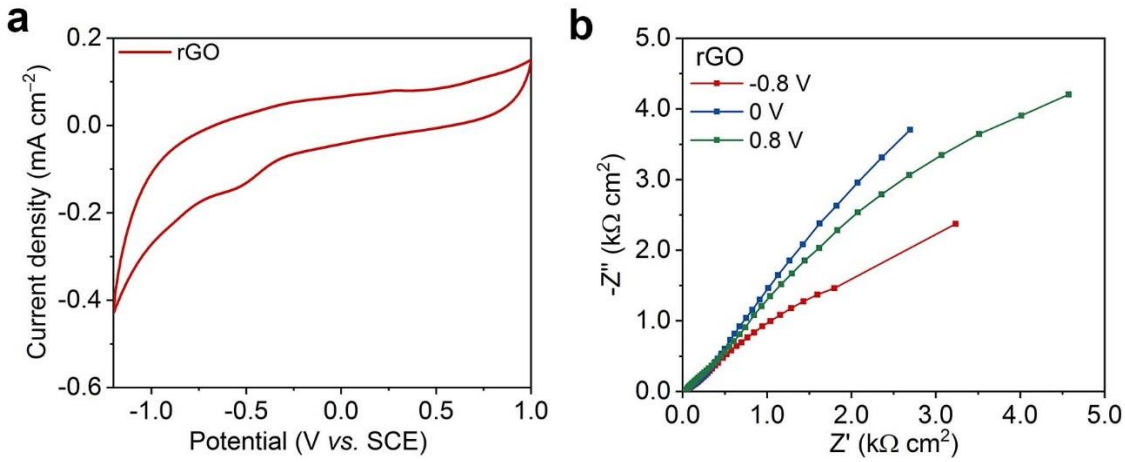

Figure S18. a, Cyclic voltammograms (CVs) of rGO electrodes at a scan rate of 50 mV s^{-1} in a three-electrode configuration with Pt plate as the counter electrode, saturated calomel electrode (SCE) as the reference electrode, and Dulbecco's phosphate buffer saline as the electrolyte. Upon the negative potential below –0.8 V, the current increased as the evolution of hydrogen evolution reactions. **b,** Electrochemical impedance spectra of rGO film at different potentials with an amplitude of 5 mV and a frequency range of 0.1-10^5 Hz.

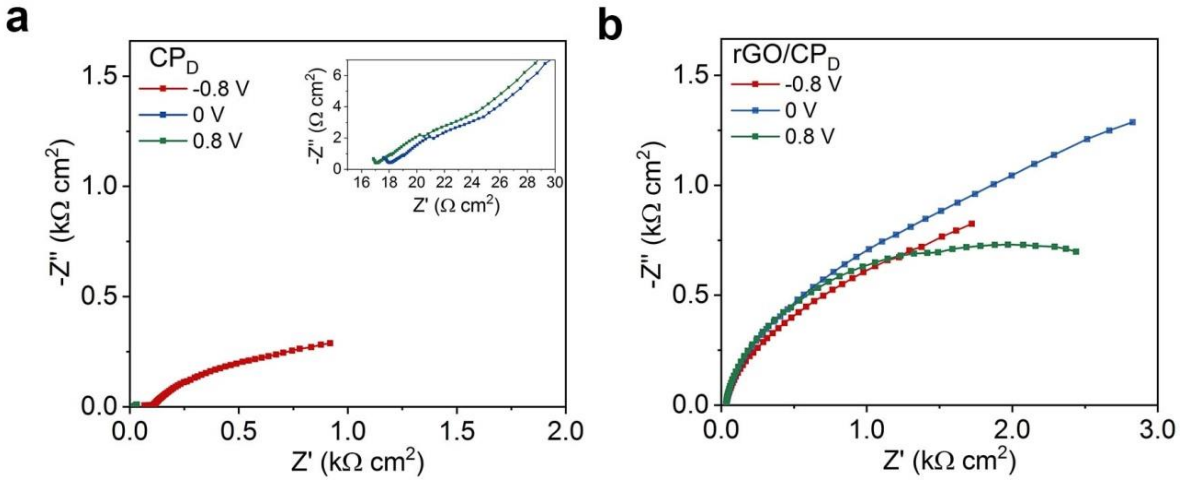

Figure S19. Electrochemical impedance spectra of CP_D and rGO/CP_D films as electrodes at different potentials with an amplitude of 5 mV and a frequency range of 0.1-10^5 Hz. The impedance spectra were recorded in a three-electrode configuration with Pt plate as the counter electrode, saturated calomel electrode as the reference electrode, and Dulbecco's phosphate buffer saline as the electrolyte.

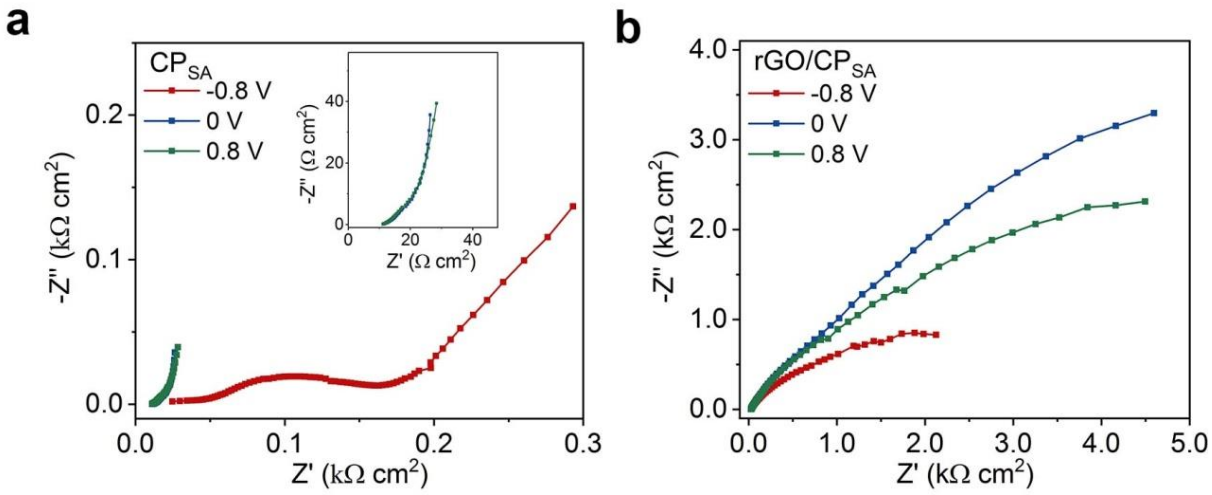

Figure S20. Electrochemical impedance spectra of CP_{SA} and rGO/CP_{SA} films as electrodes at different potentials with an amplitude of 5 mV and a frequency range of 0.1-10^5 Hz. The impedance spectra were recorded in a three-electrode configuration with Pt plate as the counter electrode, saturated calomel electrode as the reference electrode, and Dulbecco's phosphate buffer saline as the electrolyte.

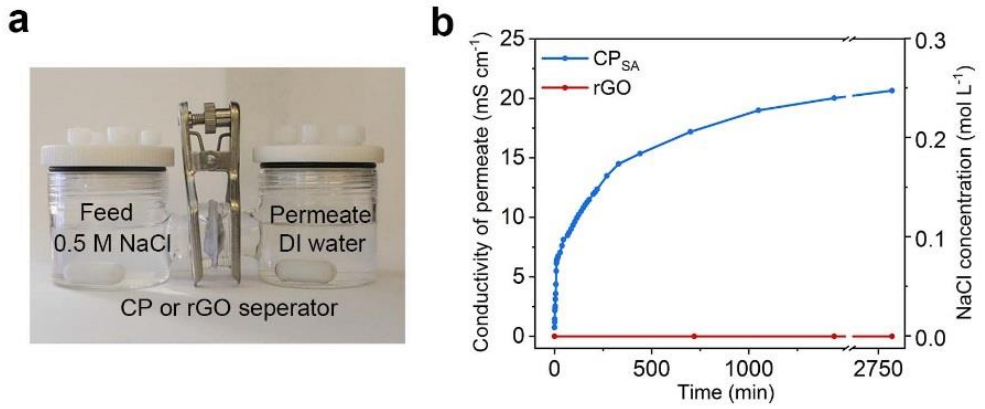

Figure S21 a, Digital photograph of the permeation test device which consists of a feed chamber, a permeate chamber and a separator between them. The conductivities of permeate were measured continuously upon the feed and permeate solutions were kept stirred. **b**, The conductivity changes of the permeate with the time when CP_{SA} or rGO was used as the separator.

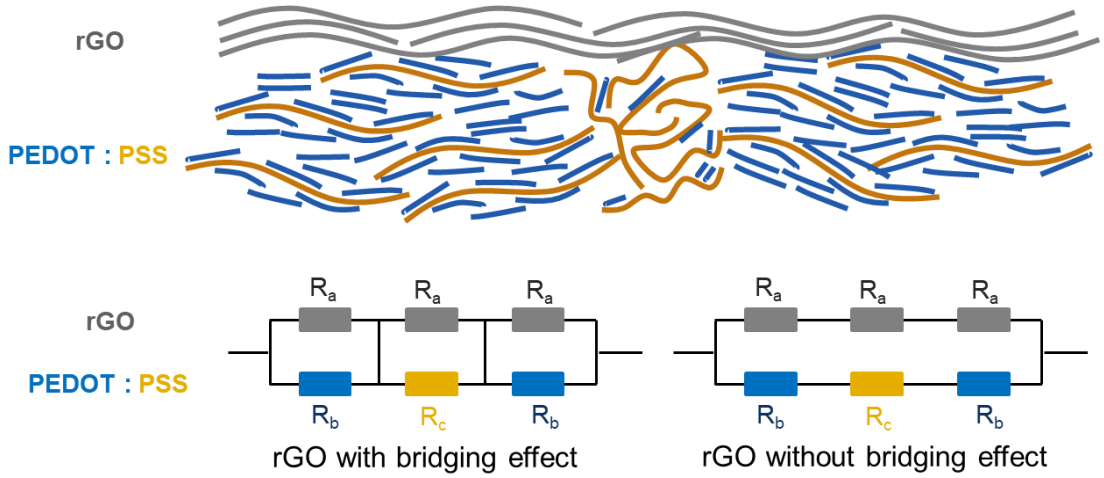

Figure S22. Schematic illustrations and two different electrical models of rGO/CP films. The rGO film acts as a bridge to connect the conductive PEDOT-rich domains separated by the less conductive PSS-rich domains. For comparison, if without bridging effect, the rGO film is considered to connect with PEDOT:PSS film in parallel.

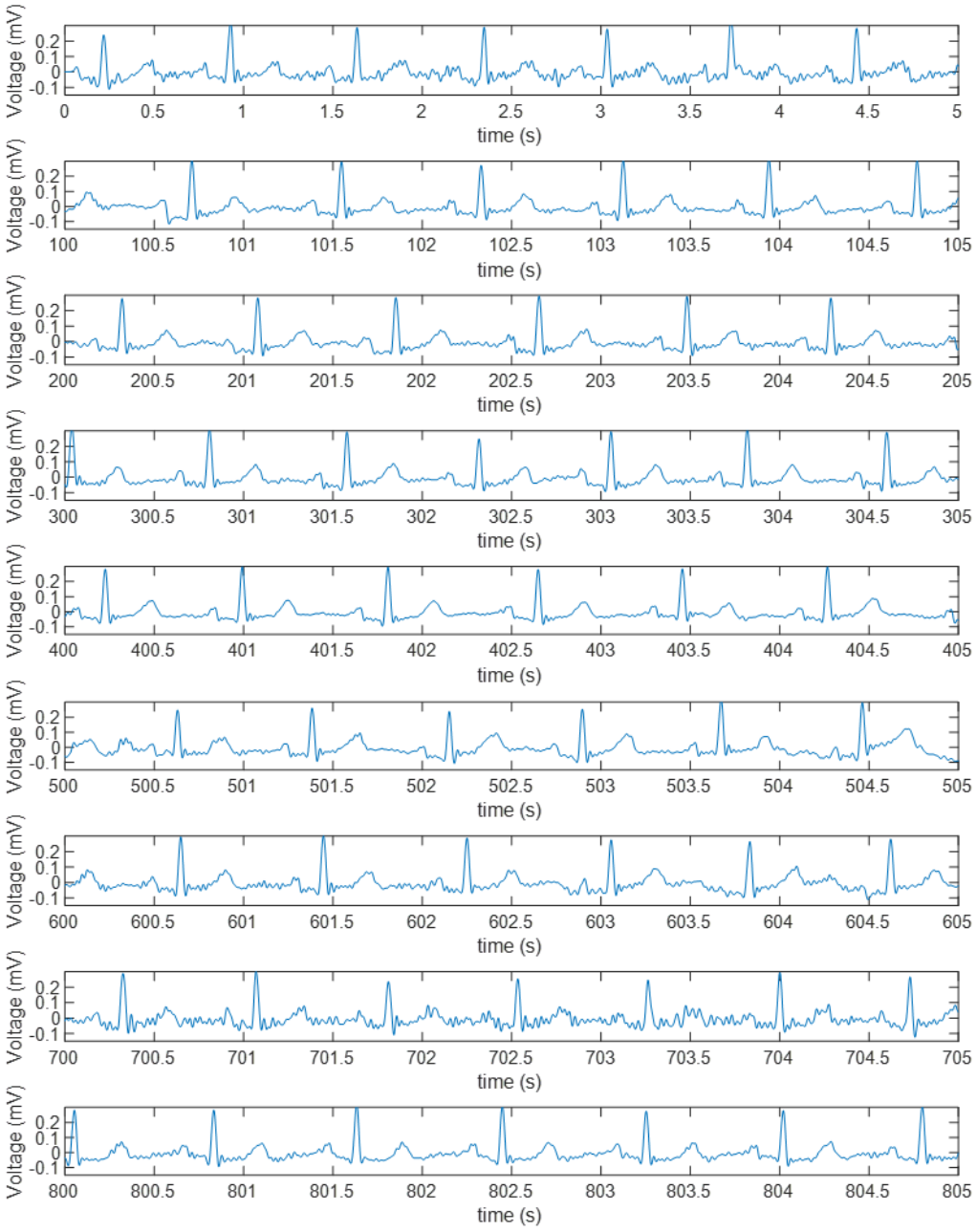

Figure S23. Representative ECG signals recorded by the rGP/CP electrodes. The ECG signals were recorded continuously for ~800 s, and the data in the first 5 seconds of every 100 s were shown here.

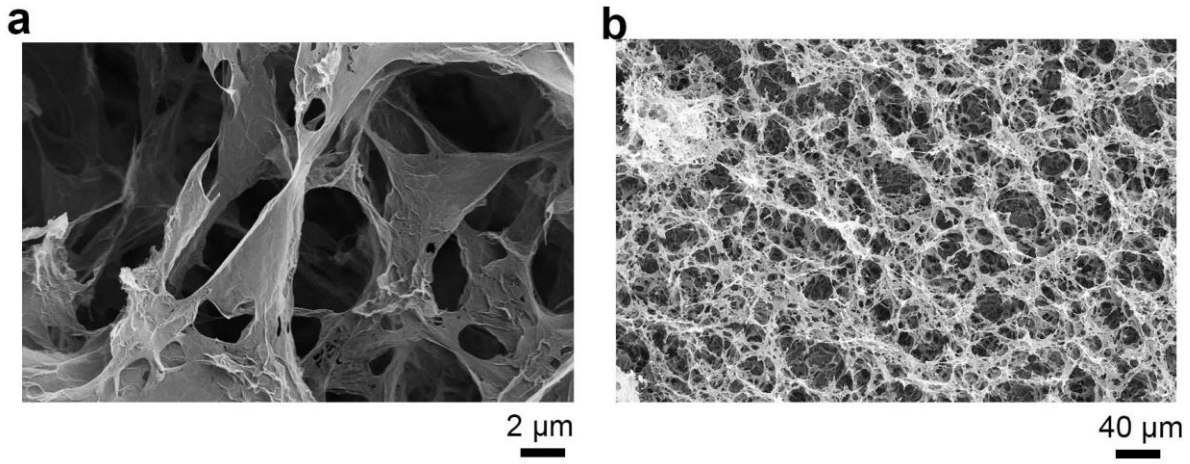

Figure S24. Scanning electron microscopy images of the PG/rGO/CP_{HI} electrodes prepared by electrodeposition under the potential of −1.2 V (*v.s.* SCE) in 3 mg mL^{-1} GO suspension containing 0.1 M $LiClO_4$ for 60 s.

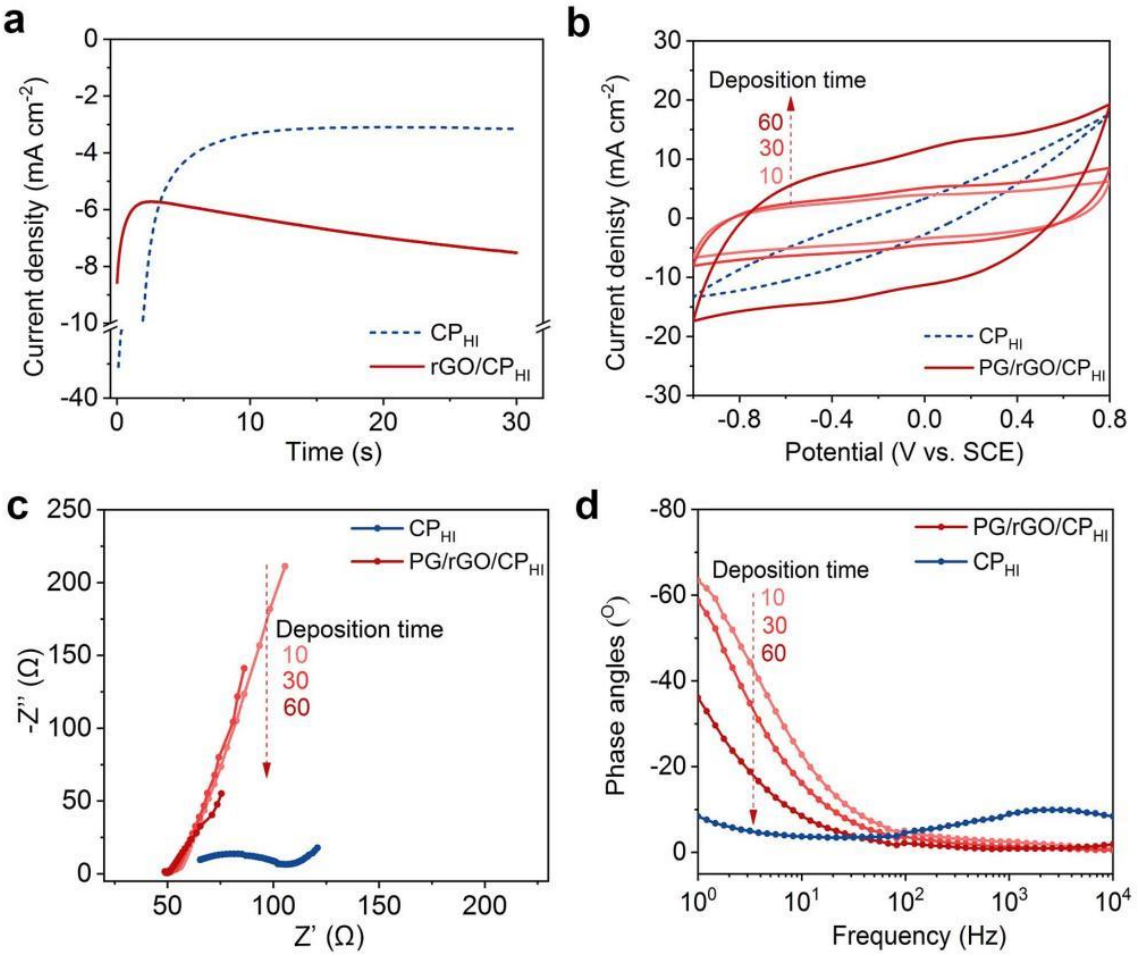

Figure S25. Preparation and electrochemical tests of various electrodes. (a) Deposition curves when CP_{HI} or rGO/CP_{HI} film was used as the current collector to deposit porous graphene in a 3 mg mL^{-1} GO suspension containing 0.1 M $LiClO_4$. (b) CVs of CP_{HI} and $PG/rGO/CP_{HI}$ at the scan rate of 1 V s^{-1} in Dulbecco's phosphate buffer saline (DPBS). CP_{HI} electrode had a resistive-like behavior, rather than a capacitive behavior, as the result of the failure of PG deposition and decrease of conductance at negative potential. (c, d) EIS of CP_{HI} and $PG/rGO/CP_{HI}$ at the potential of 0 V (*vs*. SCE) and amplitude of 5 mV.

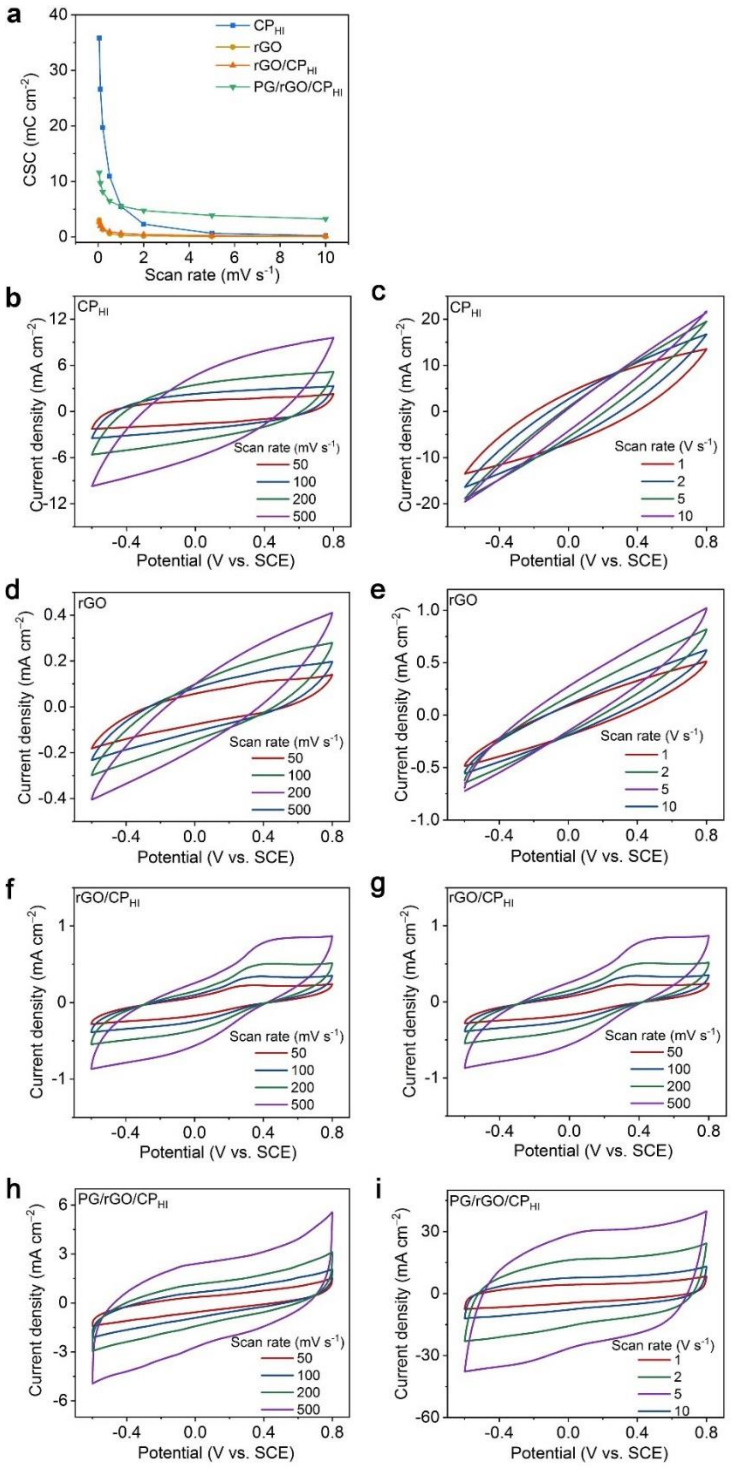

Figure S26. a, Plots of CSCs of different electrodes *vs.* scan rates from 0.05 to 10 V s^{-1} upon a fixed voltage range of −0.6-0.8 V. **b-i**, CVs of CP_{HI} (**b, c**), rGO (**d, e**), rGO/CP_{HI} (**f, g**) and PG/rGO/CP_{HI} (**h, i**) electrodes at the scan rate of 0.05-10 V s^{-1}.

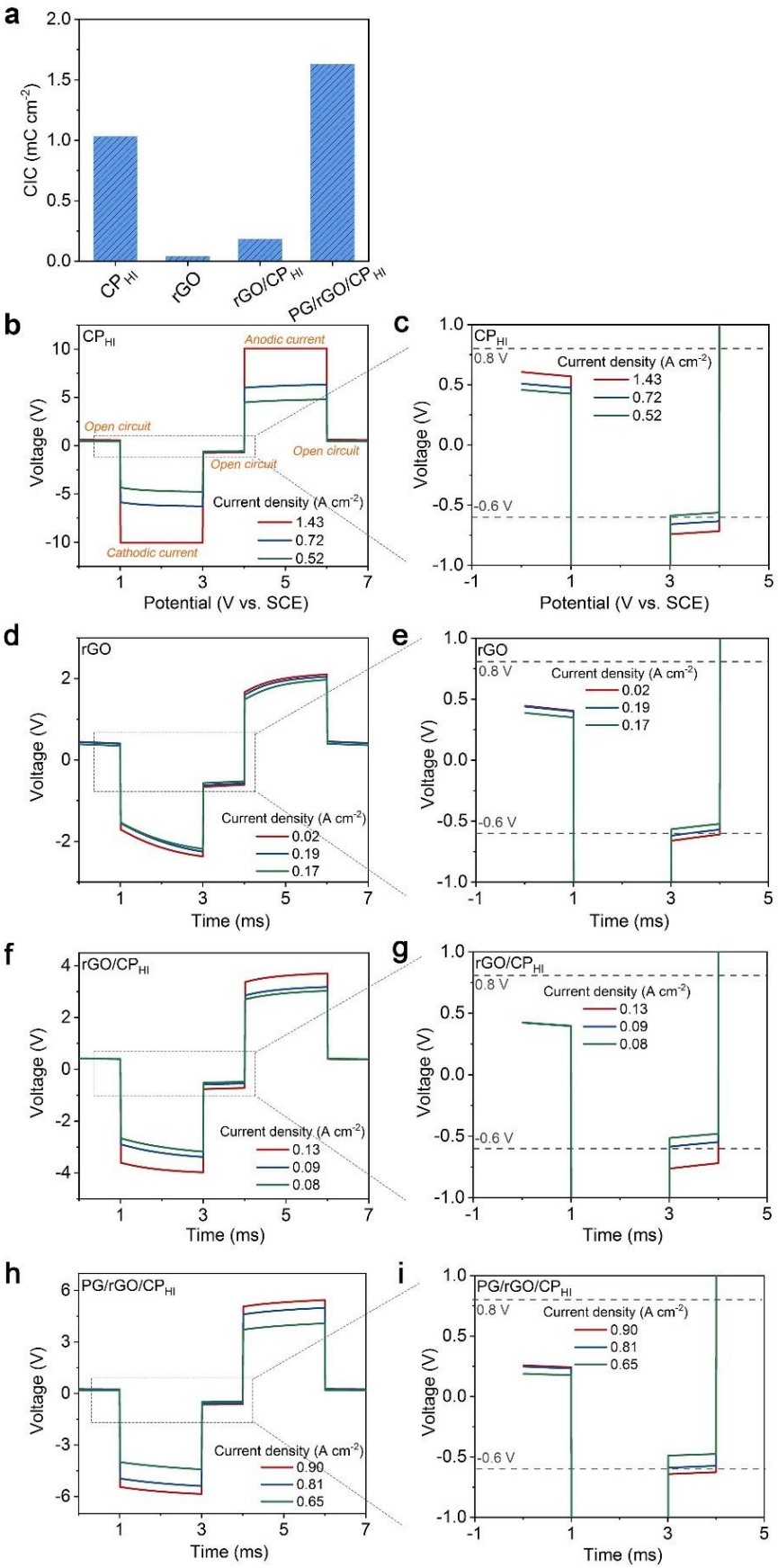

Figure S27. a, Comparisons of the CICs of different electrodes (CP_{HI}, rGO/CP_{HI}, rGO and $PG/rGO/CP_{HI}$), tested by the pulse galvanostatic method. **b-i**, Voltage-time curves of different

electrodes upon cathodal-first charge-balanced biphasic symmetric current pulse, where the cathodic and anodic square-wave currents (pulse widths of 2 ms) were applied, separated by an open circuit interval of 1 ms: CP_{HI} (**b**, **c**); rGO (**d**, **e**); rGO/CP_{HI} (**f**, **g**); PG/rGO/CP_{HI} electrodes (**h**, **i**). The panels **c**, **e**, **g** and **i** are the enlarged figures of the dashed domains in the panels **b**, **d**, **f** and **h**, respectively.